

# A Comprehensive Experimental and Kinetic Modeling Study of the Combustion Chemistry of Diethoxymethane

Sascha Jacobs, Malte Döntgen, Awad B. S. Alqaity, Raik Hesse, Stephan Kruse, Joachim Beeckmann, Leif C. Kröger, Philipp Morsch, Kai Leonhard, Heinz Pitsch, and K. Alexander Heufer\*



Cite This: <https://doi.org/10.1021/acs.energyfuels.1c01988>



Read Online

ACCESS |



Metrics & More

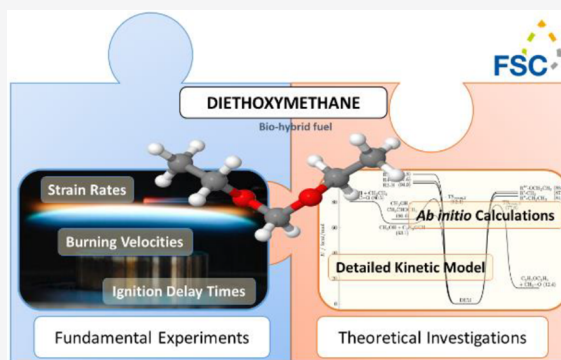


Article Recommendations



Supporting Information

**ABSTRACT:** The potential biohybrid fuel diethoxymethane (DEM) shows similar efficiency in reducing the peak mole fraction of soot precursors as oxymethylene ethers with having a higher energy density. In the present work, the fundamental combustion chemistry of DEM is studied experimentally and theoretically to obtain a comprehensive description of its combustion characteristics. A detailed kinetic model is developed to describe the pyrolysis and oxidation processes at low and high temperatures. To achieve this, rate coefficients for the unimolecular fuel decomposition and the thermal dissociation of a relevant QOOH radical are predicted from high-level *ab initio* calculations. In addition, ignition delay times of DEM have been measured in a shock tube and in a laminar flow reactor over a wide range of conditions ( $p = 1\text{--}50$  bar,  $T = 480\text{--}1170$  K, and equivalence ratios of 0.5, 1.0, and 2.0). Laminar burning velocity experiments of DEM/air mixtures have been performed in a spherical combustion vessel at an initial temperature of 398 K, at pressures from atmospheric pressure to 2.5 bar, and at equivalence ratios from 0.8 to 1.7. In addition, the experimental measurement campaign in this study was complemented with the determination of extinction strain rates for non-premixed DEM flames in a laminar counterflow burner. All of these experiments substantially extend the current database describing DEM oxidation. The validation of the newly developed model is performed with the data sets from this work and available literature. Rate of production and sensitivity analyses were performed to identify critical pathways and to understand the mechanism in more detail. In contrast to other highly reactive fuels, the characteristic of autoignition behavior of DEM is different and does not show negative temperature coefficient (NTC) behavior under the conditions investigated. The chemical reactivity at intermediate temperature of DEM is controlled by two fast  $\beta$ -scission reactions and  $\text{HO}_2$  elimination reactions.



## 1. INTRODUCTION

In previous fuel design processes dialkoxymethane ethers, especially diethoxymethane (DEM,  $\text{C}_2\text{H}_5\text{O}-\text{CH}_2\text{O}-\text{C}_2\text{H}_5$ ), have been identified as highly interesting fuel components toward clean and efficient combustion utilizing innovative engine concepts.<sup>1</sup> The energy efficient and sustainable production pathway developed in the Cluster of Excellence “Tailor-Made Fuels from Biomass” (TMFB) underlines DEM’s potential as a future fuel candidate.<sup>2,3</sup> Bio-based ethanol (EtOH) and  $\text{CO}_2$  as carbon feedstock can be combined with “green hydrogen” from water electrolysis to form DEM and thus cutting the energy-intensive oxidation of methanol to formaldehyde, which is part of the established industrial production process.<sup>4</sup> These production characteristics agree very well with the declared goals of the new Cluster of Excellence “The Fuel Science Center” (FSC) at the RWTH Aachen University.<sup>5</sup> The aim of the FSC is the integrated conversion of bio-based carbon feedstocks and  $\text{CO}_2$  with renewable electricity into high-density liquid energy carriers (“bio-hybrid fuels”). The motivation is to combine the

advantages of both biofuels and e-fuels to achieve a sustainable market for liquid transportation fuels. DEM, also called ethylal, is a diether or acetal and has a similar molecular structure to oxymethylene ethers ( $\text{OME}_x$ ,  $\text{CH}_3\text{O}-(\text{CH}_2\text{O})_x-\text{CH}_3$ ). Thus, it is expected to have an analogously favorable influence on the trade-off of NOx versus particulate matter (PM) due to its combustion behavior. Currently, there are a number of published studies regarding chemical kinetics, autoignition behavior, and emission characteristics of  $\text{OME}_x$ .<sup>6–9</sup> However, investigations of the fundamental combustion chemistry of DEM are currently limited in the literature. Investigations on the high-temperature combustion chemistry of neat DEM have been performed by Herzler et al.<sup>10</sup> and Zhang et al.<sup>11</sup> Herzler

Received: June 18, 2021

Revised: August 26, 2021

et al.<sup>10</sup> measured the decomposition of ethoxy compounds (tetraethyl orthocarbonate, diethyl carbonate, and diethoxymethane) in a single-pulse shock tube and identified ethylene and ethanol as important decomposition products leading to 1.2 and 0.5 molecules, respectively, for every DEM molecule consumed. These experiments were performed at pressures between 2 and 4 bar and in the temperature range of 1150–1260 K. Zhang et al.<sup>11</sup> measured the ignition delay times (IDTs) of highly diluted DEM/oxygen/argon mixtures in a shock tube (ST) with equivalence ratios varying from 0.5 to 2.0, at pressures of 2, 4, and 10 bar, and at temperatures higher than 1065 K. Furthermore, they also used these experimental data for the development and validation of a high-temperature kinetic model. Dias and Vandooren<sup>12</sup> studied the effect of DMM (dimethoxymethane, OME<sub>1</sub>) and DEM addition to premixed ethylene/oxygen/argon-rich flat flames by measuring species concentration profiles. The experimental results for fuel and intermediate species were found to be in good agreement to their newly developed high-temperature DEM submechanism. Besides, the overall rate coefficients of the H atom abstraction on DEM by hydroxyl radicals (OH) have been independently measured by Porter et al.<sup>13</sup> and Thüner et al.<sup>14</sup> at 298 K, respectively, and by Vovelle et al.<sup>15</sup> in a temperature range of 296–619 K. Additionally to previously mentioned experimental investigations, Kröger et al.<sup>16</sup> provided high-level *ab initio* rate constants for the H atom abstractions by hydrogen (H), methyl (CH<sub>3</sub>), and ethyl (C<sub>2</sub>H<sub>5</sub>) radicals on DEM. They also determined the thermochemistry for several key species during the DEM oxidation, i.e., fuel (RH) and primary fuel radicals (R). Furthermore, the modified Arrhenius parameters of the temperature- and pressure-dependent  $\beta$ -scission reactions as well as the thermal isomerization rate constants of the corresponding DEM radicals were calculated. Lehrheuer et al.<sup>4</sup> investigated DEM in a single-cylinder research engine and identified its potential in a lean, autoignition combustion system. In addition, the authors presented the first IDT measurements at low temperatures by studying the ignition behavior of DEM in a shock tube and a rapid compression machine (RCM) at a pressure of 30 bar, temperatures of 550–1100 K, and two different levels of dilution under stoichiometric conditions. Li et al.<sup>17</sup> have recently developed two chemical kinetic models for DEM oxidation: one modeling the chemistry from low to high temperatures and another for exclusively high temperatures with additional combustion chemistry for OME<sub>2–4</sub>. A focus of their investigations was a comparison of the autoignition characteristic between DEM and *n*-heptane under a wide range of conditions.

The present study proposes an experimental and kinetic modeling study covering the low-, intermediate-, and high-temperature oxidation pathways for a comprehensive description of DEM combustion at engine relevant conditions. Moreover, a comprehensive unimolecular decomposition mechanism including bond-fission and roaming (isomerization–decomposition) reactions is provided by using high-level quantum chemical calculations. For validation, new IDT measurements of DEM have been performed in a shock tube and in a laminar flow reactor (LFR), thereby covering a wide range of pressures, temperatures, and equivalence ratios. To further validate the present model, laminar burning velocities were measured in a spherical combustion vessel (SCV), and experiments were performed in a laminar counterflow burner (LFB) to investigate the extinction strain rates. To ensure the

model's prediction capability, the mechanism is also validated against the available literature data.<sup>4,11,12</sup>

## 2. EXPERIMENTAL METHODS

A summary of all conducted measurements including the corresponding mixture conditions and the facilities considered for the investigation is given in Table 1. For preparation of the mixture in

**Table 1. Overview of the Investigated DEM Experimental Conditions, Composition of the Gaseous Components (in mol %), and the Facilities Considered**

facility	<i>p</i> (bar)	<i>T</i> (K)	composition	measured phenomenon
shock tube (ST)	10, 50	830–1170	$\phi = 1.0$ ; O <sub>2</sub> /N <sub>2</sub> = 21/79	ignition delay times (IDT)
	30	655–1125	$\phi = 0.5, 2.0$ ; O <sub>2</sub> /N <sub>2</sub> = 21/79	
laminar flow reactor (LFR)	1.013	480–515	$\phi = 1.0$ ; O <sub>2</sub> /N <sub>2</sub> = 21/79	first stage ignition delay times
	25	485–520	$\phi = 1.0$ ; O <sub>2</sub> /N <sub>2</sub> = 15/85	
spherical combustion vessel (SCV)	1.013	398	$\phi = 0.8–1.7$	laminar burning velocities ( <i>S<sub>L</sub></i> )
	2.5		O <sub>2</sub> /(N <sub>2</sub> + Ar) = 20.94/(78.13 + 0.93)	
laminar counterflow burner (LFB)	1.013	<i>T</i> <sub>1</sub> = 405 <sup>a</sup>	<i>Y</i> <sub>F,1</sub> = 0.26–0.36 <sup>b</sup>	extinction strain rates ( <i>a<sub>2</sub></i> )
	25	<i>T</i> <sub>2</sub> = 305 <sup>a</sup>	<i>Y</i> <sub>O<sub>2</sub>,2</sub> = 0.24–0.28 <sup>c</sup>	

<sup>a</sup>*T*<sub>1</sub>: temperature of the fuel (DEM/N<sub>2</sub>) stream; *T*<sub>2</sub>: temperature of the oxidizer (O<sub>2</sub>/N<sub>2</sub>) stream. <sup>b</sup>*Y*<sub>F,1</sub>: mass fraction of DEM in the fuel stream for constant oxygen mass fraction of *Y*<sub>O<sub>2</sub>,2</sub> = 0.233. <sup>c</sup>*Y*<sub>O<sub>2</sub>,2</sub>: oxygen mass fraction in the oxidizer stream for constant fuel mass fraction of *Y*<sub>F,1</sub> = 0.28.

all facilities, the purity of DEM and gases used was higher than 99%. The experimental data sets and a detailed description of all facilities are presented as Supporting Information (sections S1 and S3); therefore, only a brief explanation will be given here.

**2.1. Shock Tube (ST).** IDT measurements for conditions as listed in Table 1 were performed in the HGD shock tube, which has been previously described in detail.<sup>18,19</sup> The IDT is defined as the time interval between the pressure rise caused by the reflected shock and the steep pressure rise corresponding to the ignition determined from the pressure history recorded by the pressure transducer (PCB 113B22) closest to the end wall (9 mm). With the recorded data (*p*<sub>1</sub>, *T*<sub>1</sub>, and incident shock velocity), the shock equations were solved with an in-house routine based on the shock and detonation toolbox<sup>20</sup> developed for Cantera<sup>21</sup> to calculate *p*<sub>5</sub> and *T*<sub>5</sub>. To determine the incident shock wave velocity, five pressure transducers are distributed over the last 1.0 m of the driven section before the closed end wall. Considering possible uncertainties in the measurement of the initial conditions (*p*<sub>1</sub>, *T*<sub>1</sub>), the shock velocities, and the thermodynamic data of the fuel/air mixtures led to a combined uncertainty in the temperatures and pressures behind the reflected shock of ±0.7% and ±1.5%, respectively.<sup>22</sup> Furthermore, the shock attenuation becomes important for longer IDTs, and an average constant pressure rise of *dp/dt* = 7%/ms was identified before autoignition events.<sup>23</sup> This effect has been included in all ST simulations by considering an effective change in volume in the 0-D simulations.<sup>23</sup> The mixtures were premixed in a stainless steel vessel by monitoring partial pressures with two static pressure transducers. The ST with the corresponding attached manifold, including mixing vessels, is equipped with an electrical heating system to avoid condensation of the fuel. The overall

Table 2. Calculated Modified Arrhenius Parameters for the Unimolecular Decomposition of DEM

reaction	A (cm <sup>3</sup> /mol/s)	n	E <sub>a</sub> (cal/mol)
DEM $\rightleftharpoons$ $\dot{\text{C}}\text{H}_3 + \text{C}_2\text{H}_5\text{OCH}_2\text{O}\dot{\text{C}}\text{H}_2$	$2.743 \times 10^{23}$	-1.762	90856.2
DEM $\rightleftharpoons$ $\dot{\text{C}}_2\text{H}_5 + \text{C}_2\text{H}_5\text{OCH}_2\dot{\text{O}}$	$2.359 \times 10^{27}$	-3.160	86810.6
DEM $\rightleftharpoons$ $\text{C}_2\text{H}_5\dot{\text{O}} + \text{C}_2\text{H}_5\text{O}\dot{\text{C}}\text{H}_2$	$2.437 \times 10^{26}$	-2.981	89993.9
DEM $\rightarrow$ $\text{C}_2\text{H}_5\text{OH} + \text{C}_2\text{H}_4 + \text{CH}_2\text{O}$	$8.404 \times 10^5$	1.631	79549.2
DEM $\rightleftharpoons$ $\text{C}_2\text{H}_5\text{OC}_2\text{H}_5 + \text{CH}_2\text{O}$	$1.169 \times 10^9$	0.779	76471.9
DEM $\rightarrow$ $\text{C}_2\text{H}_5\text{OH} + \dot{\text{C}}_2\text{H}_5 + \text{H}\dot{\text{C}}\text{O}$	$3.062 \times 10^{10}$	1.135	69598.6
DEM $\rightleftharpoons$ $\text{C}_2\text{H}_5\text{OCH}_2\text{OCH}_2\dot{\text{C}}\text{H}_2 + \dot{\text{H}}$	$1.792 \times 10^{16}$	-0.032	104357.6
DEM $\rightleftharpoons$ $\text{C}_2\text{H}_5\text{OCH}_2\text{O}\dot{\text{C}}\text{HCH}_3 + \dot{\text{H}}$	$3.026 \times 10^{16}$	-0.161	97690.7
DEM $\rightleftharpoons$ $\text{C}_2\text{H}_5\text{O}\dot{\text{C}}\text{HOC}_2\text{H}_5 + \dot{\text{H}}$	$1.406 \times 10^{18}$	-0.712	99325.3

measurement scatter for measured IDT is estimated to be within a range of  $\pm 20\%$ .<sup>24</sup>

**2.2. Laminar Flow Reactor (LFR).** For temperatures below 520 K, the ITV laminar flow reactor (LFR) was used in which the first stage ignition delay times could be determined. The LFR used in this study has previously been discussed in detail in ref 25. The investigation was performed for stoichiometric DEM/O<sub>2</sub>/N<sub>2</sub> mixtures at atmospheric pressure. The quartz tube LFR with an inner diameter of 20.6 mm is placed in an oven to maintain close to isothermal condition across its length. The helical reactor is fitted with 48 type-N thermocouples at regular intervals of 89 mm along its length of 4800 mm. First stage ignition location is identified by the axial position of the thermocouple showing peak temperature and is subsequently converted to derived ignition delay time by using a conversion factor (details in ref 26). The conversion factor is defined as the ratio of ignition location normalized by inlet velocity to the zero-dimensional ignition delay time and depends on the reactivity of the fuel/oxidizer mixture.

**2.3. Spherical Combustion Vessel (SCV).** Laminar flame speed experiments for conditions as listed in Table 1 are performed in ITV's spherical combustion vessel (SCV)<sup>27</sup> equipped with an optical Schlieren cinematography setup. A dual-field Schlieren arrangement<sup>28</sup> is combined with a high-speed CMOS camera (LaVision High-SpeedStar 6) and applied to capture the outward location of the propagating flame. Flame images of 448  $\times$  448 pixels are recorded at a rate of 25000 frames/s and resolve each millimeter with 10.68 pixels. The mixtures are prepared in an insulated and heated premixing vessel by using the partial pressure method. The pressure in the premixing and combustion vessel is monitored via separate Keller 35 X HTC transducers. The combined measurement uncertainty in the flame speed depending on the mixture accuracy, and the initial pressure and temperature are below 4%. Flame speeds were extracted only of spherically smooth flame fronts in a constraint regime, associated on the lower end with the complete decay of ignition effects and on the upper end with a pressure increase above 2%, violating quasi-isobaric combustion.<sup>29,30</sup>

Extrapolation deviations between the unstretched flame speed  $s_0$  from both linear<sup>31,32</sup> and nonlinear<sup>33</sup> models are interpreted as additional uncertainty. Combining the individual standard uncertainties according to GUM<sup>34</sup> and applying a coverage factor of 2 yields the extended uncertainty of 5% for the majority of measured conditions. Only atmospheric pressure lean flames possess an uncertainty up to 9% due to the more pronounced extrapolation uncertainty.

**2.4. Laminar Counterflow Burner (LFB).** The counterflow configuration from the ITV was used to determine the extinction strain rates of DEM. The setup has been frequently used for extinction strain rate measurements of gaseous fuels<sup>35</sup> and soot investigation of gasoline surrogate components.<sup>36</sup> The laminar counterflow burner (LFB) consists of two opposed contoured stainless-steel ducts in a vertical arrangement. The oxidizer was issued through the top nozzle, while the nitrogen-diluted fuel stream was provided through the bottom nozzle, with a distance of 10 mm between the two nozzles. Honeycombs and layers of wired meshes were mounted 200 and 1 mm upstream of each nozzle exit, respectively, to achieve a top-hat velocity profile. Thermocouples are

located immediately upstream of the wired mesh layers to monitor gas stream temperatures. To avoid the entrainment of ambient air to the fuel and oxidizer stream, a nitrogen coflow stream was used as a shielding flow. All gaseous flows and DEM were controlled and monitored by mass flow controllers. For this campaign, an oxidizer and fuel/N<sub>2</sub> stream were kept in momentum balance. The strain rate was gradually increased in steps of 5 s<sup>-1</sup> until local extinction of the flame was observed.

### 3. COMPUTATIONAL METHODS

To improve the model's prediction quality, this study also provides new quantum chemical calculations of rate coefficients for crucial reactions.

**3.1. Ab Initio Calculations.** A theoretical study was performed for six possible unimolecular decomposition reactions and three carbon–hydrogen unimolecular dissociation reactions leading to the formation of the corresponding DEM radical and one H radical. Furthermore, the present model also provides high-level *ab initio* reaction rate constants for the dissociation kinetics of a relevant hydroperoxy fuel radical: C<sub>2</sub>H<sub>5</sub>OCHOCH(OOH)CH<sub>3</sub>, labeled Q2OOHc (the number refers to the position of the hydroperoxide group and the letter to the radical position). The resulting high-pressure limit rate parameters for the modified Arrhenius equation are summarized in Tables 2 and 3. The calculations were performed at the B3LYP-D3BJ/def2-TZVP<sup>37,38</sup> level of theory for molecular structures, harmonic frequencies, and one-dimensional hindered rotor profiles. Single point energy (SPE) calculations were performed at the DLPNO-CCSD-(T)/CBS<sup>39,40</sup> level of theory by using the cc-pVTZ and cc-pVQZ basis sets according to  $E_{\text{CBS}} = (4^3 \times E_{\text{QZ}} - 3^3 \times E_{\text{TZ}}) / (4^3 - 3^3)$ .<sup>41</sup> The ORCA software package<sup>42</sup> was used for all calculations, except for the Q2OOHc  $\beta$ -scission transition state structure, harmonic frequencies, and one-dimensional hindered rotor profiles, which were obtained by using the Gaussian software package (TZVP instead of def2-TZVP basis set).<sup>43</sup> The largest T1 diagnostic relevant for DEM dissociation amounts to 0.0195, which is slightly below the generally accepted threshold of 0.02 for closed-shell systems.

The DEM pyrolysis rate coefficients were predicted via Rice–Ramsperger–Kassel–Marcus theory (RRKM)/master equation (ME) simulations conducted via the MESS software package.<sup>44</sup> Collisional energy transfer was modeled via the Lennard-Jones (LJ) collision frequency model and the exponential-down model  $\langle \Delta E \rangle_{\text{down}} = 200 \text{ cm}^{-1} \times (T/300 \text{ K})^{0.85}$ . The LJ parameters for DEM were obtained via group additivity as implemented in the RMG software package<sup>45</sup> ( $\epsilon = 330 \text{ K}$  and  $\sigma = 6.2 \text{ \AA}$ ). The LJ parameters of the bath gas (N<sub>2</sub>) are taken from the study of Tee et al.<sup>46</sup> ( $\epsilon = 85.2 \text{ K}$  and  $\sigma = 3.7 \text{ \AA}$ ). A relevant pyrolysis pathway leads to the products ethanol (EtOH) and ethoxymethylene (C<sub>2</sub>H<sub>5</sub>O $\dot{\text{C}}\text{H}$ ). Ethoxymethylene



is a stable singlet intermediate, which easily decomposes to ethyl and formyl radicals. The ethoxymethylene LJ parameters were estimated via group additivity ( $\epsilon = 311$  K and  $\sigma = 5.2$  Å). However, this calculated two-step unimolecular decomposition is combined into a lumped reaction in the mechanism.

A short-cut approach was used to describe the C–H, C–C, and C–O bond fission kinetics of DEM: The bond dissociation energy profile was calculated as Morse oscillator according to  $V_{\text{Morse}}(r) = D_{\text{E}}(1 - \exp(-\alpha(r - r_0)))^2$ , with the dissociation threshold  $D_{\text{E}}$ , the curvature parameter  $\alpha$ , the bond coordinate  $r$ , and the equilibrium bond length  $r_0$ . The dissociation threshold is equal to the bond dissociation energy (BDE) of the respective bond, and the equilibrium bond length is the average of all equilibrium bond lengths of indistinguishable bonds of the energy-minimized molecular geometry. The curvature parameter is calculated from the harmonic oscillator frequency  $\nu_0$ , averaged over those of all bond stretching modes of indistinguishable bonds, and the dissociation threshold according to  $\alpha = 2\pi\nu_0 \sqrt{\mu/2 \times D_{\text{E}}}$ , with  $\mu$  being the averaged reduced mass of the bond stretching of indistinguishable bonds. The Morse oscillator bond dissociation profile is converted into the attractive potential  $V_{\text{attr}}(r) = a/r^b$ , which is used for solving the phase space theory (PST) number of states in the MESS software package.<sup>44</sup> This conversion is based on the bond lengths of the Morse potential evaluated at 30% and 50% of the Morse dissociation threshold  $D_{\text{E}}$ . Various combinations of percentage  $D_{\text{E}}$  have been tested, and the 30%/50% combination was found to reproduce the experimental rate coefficient of Herzler et al.<sup>10</sup> best. A comparison of the presently predicted and Herzler's experimentally determined rate coefficients for the unimolecular decomposition reaction  $\text{DEM} \rightleftharpoons \text{C}_2\text{H}_5\text{OCH}_2\dot{\text{O}} + \text{C}_2\text{H}_5$  is discussed in the Supporting Information (section S5.1.2). The recently published study of Lizardo-Huerta et al.<sup>47</sup> showed that the isomerization–decomposition reaction of diethyl ether leading to ethanol cleavage is dominant over the simple bond fission reaction at low temperatures. However, the C–O bond fission reaction becomes competitive with increasing temperature (above 1200 K). Our *ab initio* calculations can reflect exactly this behavior for DEM. A comparison of high-pressure limit rate coefficients between reactions  $\text{DEM} \rightleftharpoons \text{C}_2\text{H}_5 + \text{C}_2\text{H}_5\text{OCH}_2\dot{\text{O}}$  and  $\text{DEM} \rightarrow \text{C}_2\text{H}_5\text{OH} + \dot{\text{C}}_2\text{H}_5 + \text{HCO}$  is given as Supporting Information (Figure S22).

In the low- and intermediate-temperature chemistry of DMM combustion, the  $\beta$ -scission reaction of the QOOH radical  $\text{CH}_3\text{O}\dot{\text{C}}\text{HOCH}_2\text{OOH}$  turned out to be highly relevant for predicting ignition delay times.<sup>18</sup> For DEM, the analogous bond dissociation reaction of Q2OOHc was calculated by using the above-described levels of theory and RRKM/ME simulations. The Q2OOHc's LJ parameters were estimated via group additivity ( $\epsilon = 284$  K and  $\sigma = 6.8$  Å). This ME formulation for Q2OOHc is a simple single-well/single-channel system and cannot reflect the actual pressure dependence due to missing competing channels. The dissociation of Q2OOHc is included as a lumped reaction in the mechanism taking into account the calculated  $\beta$ -scission reaction and the fast, subsequent decomposition of the hydroperoxyethyl radical ( $\text{CH}_3\dot{\text{C}}\text{HOOH} \rightleftharpoons \text{CH}_3\text{CHO} + \text{OH}$ ). As recently published literature indicates that pressure-dependent rate coefficients do not affect the performance of the model above atmospheric pressure at low temperatures,<sup>48–51</sup> this simplification appears to be valid. All calculated rate constants for the unimolecular decomposition

and the  $\beta$ -scission reaction of Q2OOHc are also visualized in the Supporting Information (section S5.1.1).

**Table 3. Calculated Modified Arrhenius Parameters for the Thermal  $\beta$ -Scission Rate Constants of Q2OOHc Radicals of DEM**

reaction	$A$ ( $\text{cm}^3/\text{mol/s}$ )	$n$	$E_{\text{a}}$ (cal/mol)
$\text{C}_2\text{H}_5\text{O}\dot{\text{C}}\text{HOCH}(\text{OOH})\text{CH}_3 \rightarrow \text{C}_2\text{H}_5\text{OCHO} + \text{CH}_3\text{CHO} + \dot{\text{O}}\text{H}$	$1.368 \times 10^{12}$	0.081	13737.9

**3.2. Thermochemistry Data.** Thermodynamic properties including enthalpies, entropies, and heat capacities are essential for the simulation of the oxidation and pyrolysis pathways of DEM. The thermochemical parameters for DEM (RH) and its three radicals (primary C–C site:  $\dot{\text{R}}1 = \text{C}_2\text{H}_5\text{OCH}_2\text{OCH}_2\dot{\text{C}}\text{H}_2$ ; secondary C–C site:  $\dot{\text{R}}2 = \text{C}_2\text{H}_5\text{OCH}_2\text{O}\dot{\text{C}}\text{HCH}_3$ ; and central O–C–O site:  $\dot{\text{R}}4 = \text{C}_2\text{H}_5\text{O}\dot{\text{C}}\text{HOC}_2\text{H}_5$ ) are taken from the theoretical investigation of Kröger et al.<sup>16</sup> Furthermore, for the fuel fragments generated during the unimolecular decomposition and for the three fuel peroxy radicals ( $\text{RO}_2$ ) relevant to the low-temperature oxidation, the parameters were adopted from the theoretical work of Döntgen et al.<sup>52</sup> The structure of DEM with the assignment of the corresponding radical positions and bond strength is shown in Figure 1. The naming convention in this

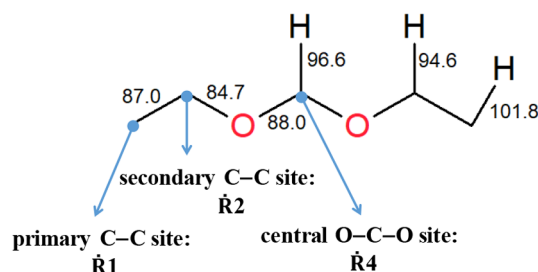


**Figure 1.** Bond dissociation energies (BDEs) of diethoxymethane calculated at 0 K. Units: kcal/mol.

work will follow the indicated numbering of the carbon atoms. The bond dissociation energies (BDEs) of DEM were calculated at the same high level of theory as in both previously mentioned refs 16 and 52. The thermochemical data of the other relevant radicals and stable parents in the submechanism are estimated by using THERM software,<sup>53</sup> which is based on the Benson group additivity theory, or are taken from the available literature.<sup>18,54–57</sup> An overview over all species, their naming as written in the submechanism for DEM, their molecular structure, and their source for the thermodynamic data is provided in the Supporting Information (section S5.3). The  $\text{C}_0$ – $\text{C}_4$  species' thermodynamic parameters were taken from the base mechanism.<sup>58</sup>

#### 4. CHEMICAL KINETIC MODEL DEVELOPMENT

In this study, a detailed kinetic model that includes both high- and low-temperature pathways has been developed for a more comprehensive description of the chemical oxidation mechanism of DEM. The new submechanism consists of 539 reactions and 123 species. The chemistry of  $\text{C}_0$ – $\text{C}_4$  molecules is taken from the NUIG0.9 version<sup>58</sup> as the base mechanism. The reaction rate constants for DEM are mainly based on

analogies to diethyl ether (DEE), dimethoxymethane (DMM), and *n*-heptane and are complemented with *ab initio* calculations where available.

Analogies to DEE and DMM have been adopted from Sakai et al.<sup>54</sup> and Yasunaga et al.<sup>59</sup> for DEE as well as from the theoretical works of He et al.<sup>7</sup> and Vermeire et al.,<sup>8</sup> and the values recommend by Jacobs et al.<sup>18</sup> for DMM. Analogies to rate constants of *n*-heptane have been drawn to the recent detailed kinetic mechanisms of Zhang et al.<sup>19</sup> Furthermore, high-level *ab initio* reaction kinetic data for several key reactions provided by Kröger et al.<sup>16</sup> are used in this study.

A detailed elucidation of the used analogies in the newly developed DEM mechanism will be described in the following sections. In general, the kinetic model features the reaction classes defined for regular alkanes, which are based on the model formulation recently revised by Bugler et al.<sup>48</sup> For a complete list of all reaction classes considered in this work, including their class ID, refer to [Tables S6 and S7](#).

The newly developed model (chemical kinetics, thermodynamics, and transport properties) is provided in CHEMKIN format and available as [Supporting Information](#).

**4.1. Reaction Rate Coefficients.** Elementary reactions are typically divided into a high- and low-temperature regime class, based on their occurrence. In the following, the major reaction classes in the submechanism of DEM are explained. Furthermore, each elementary reaction in the DEM submodel is commented in the mechanism file with the corresponding analogy and the reference as well as the modifications.

**High-Temperature Chemistry. 4.1.1. Unimolecular Decomposition (Reaction Class 1).** For DEM, six possible unimolecular decomposition reactions are considered. In addition to simple bond fission kinetics, more complex isomerization–decomposition pathways (roaming reactions) leading to the formation of EtOH and DEE are proposed. The pressure-dependent rate constants have been determined by using *ab initio* methods (cf. [section 3.1](#)).

The carbon–hydrogen unimolecular dissociation reactions lead to the formation of the three DEM fuel radicals. Because the BDEs of all C–H cleavage are higher compared to the C–C and C–O bond strengths, it can be assumed that the unimolecular fuel decomposition reactions producing a DEM radical and one H radical are not favored. The C–H cleavage is conventionally only important at very high temperatures and is considered for a comprehensive description of the kinetics of DEM in this study.

**4.1.2. H Atom Abstraction Reactions (Reaction Class 2).** The rate constants for the hydrogen atom abstraction reactions at the primary side by the major radicals O<sub>2</sub>,  $\dot{\text{O}}$ , HO<sub>2</sub>, CH<sub>3</sub> $\dot{\text{O}}$ , CH<sub>3</sub> $\dot{\text{O}}_2$ , and OH were estimated from the rate coefficients of *n*-heptane.<sup>19</sup> The reaction parameters for the secondary C–C site of DEM have been determined in analogy to the rate constants of the H atom abstraction on the primary radical position of DMM (CH<sub>3</sub>OCH<sub>2</sub>OCH<sub>2</sub>) applying the ratio between the secondary and primary position in the *n*-heptane mechanism by Zhang et al.<sup>19</sup> The rate parameters for the H atom abstractions from the central carbon and for the secondary site of DEM have been adopted from the corresponding DMM reactions based on the recommendation by Jacobs et al.<sup>18</sup> Among the most sensitive reactions for DEM, one can find the H atom abstraction reactions by OH radicals. At low temperatures, the trend of the overall rate determined with this methodology is similar to the rate constants measured by Vovelle et al.<sup>15</sup> However, to obtain a better agreement

between simulated and measured IDTs, the A-factor for the H atom abstraction by OH leading to R4 radicals has been increased by 40%. H atom abstractions by hydroperoxyl radicals (HO<sub>2</sub>) have only little impact on the fuel consumption at low temperatures, but these reactions become more important at temperature above 800 K. A factor of 2 has been applied to the A-factor of the reaction leading to R2 radicals of DEM to improve the model prediction of IDTs from intermediate to high temperatures. The rate constants for H atom abstraction by CH<sub>3</sub> $\dot{\text{O}}_2$  radicals have not yet been calculated for neither DEM nor DMM in previous studies. In the DMM submechanism by Jacobs et al.<sup>18</sup> the A-factor has been decreased by 20% compared to the abstraction by HO<sub>2</sub> radicals, reflecting the lower reactivity of the methylperoxyl radicals. Hence, these rate coefficients were implemented in the HGD DEM model for the H atom abstraction at the central position. The H atom abstraction reactions by other radical species, i.e.,  $\dot{\text{R}}$ , RO<sub>2</sub>,  $\dot{\text{O}}_2\text{CHO}$ ,  $\dot{\text{O}}\text{CHO}$ , C<sub>2</sub>H<sub>5</sub> $\dot{\text{O}}$ , and  $\dot{\text{C}}_2\text{H}_3$  were assigned by analogy with DEE or DMM. For the H atom abstraction by  $\dot{\text{H}}$ ,  $\dot{\text{C}}\text{H}_3$ , and  $\dot{\text{C}}_2\text{H}_5$ , the theoretically calculated rate parameters of Kröger et al.<sup>16</sup> are used for all abstraction sites.

**4.1.3. Fuel Radical Decomposition and Related Reactions (Reaction Classes 3–9).** Kröger et al.<sup>16</sup> calculated the  $\beta$ -scission reactions for all DEM radicals, and the fuel radicals' isomerization reactions and the corresponding high-pressure limit rate coefficients were implemented in the kinetic model.

The rate coefficients for the group of reactions producing the species C<sub>2</sub>H<sub>5</sub>OCH<sub>2</sub>OC<sub>2</sub>H<sub>3</sub> and HO<sub>2</sub> radicals (reaction class 4:  $\dot{\text{R}} + \text{O}_2 \rightleftharpoons \text{alkene} + \text{HO}_2$ ) are adopted according to the reactions from the *n*-heptane mechanism,<sup>19</sup> since these are not available in previous DEE works.<sup>54,59</sup> This class of reactions is irrelevant for the fuel radical R4, as it has no neighboring C–C bonds.

The reaction rates of all remaining reactions classes 6–9 are estimated based on analogies to DEE,<sup>54,59</sup> DEM,<sup>16</sup> DMM,<sup>60</sup> *n*-heptane,<sup>19</sup> and others<sup>19,56,60,61</sup> and are referenced correspondingly in the mechanism file as well as in the [Supporting Information](#) (cf. Table S6).

**Low-Temperature Mechanism. 4.1.4. Addition to O<sub>2</sub> (Reaction Classes 10 and 22).** In the low-temperature oxidation mechanism, the rate constants for the addition reactions  $\dot{\text{R}} + \text{O}_2$  and QOOH + O<sub>2</sub> are determined with the same methodology used for the H atom abstraction reactions. The rate parameters for the reaction involving the ethoxy side chains were determined by using the addition of molecular oxygen to the primary site of DMM recommended by Jacobs et al.<sup>18</sup> as well as to the primary and secondary radical positions of *n*-heptane proposed by Zhang et al.<sup>19</sup> The values for the rate coefficients of the addition to O<sub>2</sub> on the central carbon side of DEM are assigned according to the corresponding reaction in the DMM submechanism by Jacobs et al.<sup>18</sup>

**4.1.5. RO<sub>2</sub>  $\rightleftharpoons$  QOOH Isomerization and Related Reactions (Reaction Classes 12 and 12A).** With regard to the internal isomerization reaction, the primary peroxy fuel radicals of DEM (R1O<sub>2</sub>: C<sub>2</sub>H<sub>5</sub>OCH<sub>2</sub>OC<sub>2</sub>H<sub>4</sub>OO) can generate hydroperoxy fuel radicals QOOH via two different internal H atom transfer pathways. The rate constants for internal isomerization reactions of R1O<sub>2</sub> into Q1OOHb (C<sub>2</sub>H<sub>5</sub>OCH<sub>2</sub>O-CHCH<sub>2</sub>OOH) and Q1OOHc (C<sub>2</sub>H<sub>5</sub>OCHOC<sub>2</sub>H<sub>4</sub>OOH) have been assigned in analogy to the corresponding isomerization reactions of DEE involving a five- and a seven-membered transition state (TS) ring.<sup>54</sup>

A similar method was applied to estimate the rate constants for the internal hydrogen shift reactions with the hydroperoxide group on the secondary site of DEM, labeled Q2OOH. The internal isomerization to Q2OOHa ( $\text{C}_2\text{H}_5\text{OCH}_2\text{OCH}(\text{OOH})\text{CH}_2$ ) and Q2OOHc ( $\text{C}_2\text{H}_5\text{OCHOCH}(\text{OOH})\text{CH}_3$ ) can proceed via a five- and a six-membered TS ring at the primary and central site, respectively. For these two reactions, the rate parameters of the corresponding isomerization reactions of DEE have been adopted.<sup>54</sup> Furthermore, the formation of Q2OOHd ( $\text{CH}_3\dot{\text{C}}\text{HOCH}_2\text{OCH}(\text{OOH})\text{CH}_3$ ) can result from an internal hydrogen shift via an eight-membered TS ring. The rate coefficients for this reaction are deduced from the corresponding isomerization reaction of DMM.<sup>8</sup> However, the A-factor is multiplied by a factor of 2/3 to take into account the different number of H atoms available for abstraction. Additionally, the activation energy was reduced by 1 kcal/mol to account for the weaker C–H bond on the secondary site of DEM compared to the C–H BDE on the primary site of DMM (94.6 kcal/mol (cf. present work) vs 95.67 kcal/mol (ref 18)).

The rate constants for the formation of Q4OOHa ( $\text{C}_2\text{H}_5\text{OCH}(\text{OOH})\text{OCH}_2\dot{\text{C}}\text{H}_2$ ) and Q4OOHb ( $\text{C}_2\text{H}_5\text{OCH}(\text{OOH})\text{OCHCH}_3$ ) radicals were determined in analogy to DEE with the hydroperoxide group on the secondary site.<sup>54</sup> They are increased by a factor of 2 compared to the corresponding isomerization reactions in DEE to account for twice the amount of abstraction sites in the case of DEM.

Finally, R1O<sub>2</sub> and R2O<sub>2</sub> radicals can produce an unsaturated molecule and HO<sub>2</sub> via a concerted elimination reaction (reaction class 12a). The reaction rates are adopted by using analogies for the same type of reactions from Sakai's DEE mechanism.<sup>54</sup>

**4.1.6. QOOH Decomposition and Related Reactions (Reaction Classes 19–21).** In addition to the aforementioned second addition to O<sub>2</sub> that forms O<sub>2</sub>QOOH, QOOH radicals can react toward cyclic ether formation or β-scission.

A three- and a five-membered cyclic ether formation is considered for Q1OOHb and Q1OOHc, respectively (reaction class 19). The rate parameters for Q2OOHa and Q2OOHc involving a three- and a four-membered ring are based on analogies to the formation of 2-ethoxyoxirane and 2,4-dimethyl-1,3-dioxetane from the DEE submechanism.<sup>54</sup> Furthermore, a third reaction channel is implemented for the cyclic ether formation reaction of the Q2OOHd radical via a six-membered ring TS. The rate coefficients for this reaction have been adopted from the cyclic ether formation leading to 1,3,5-trioxane and hydroxyl radicals from the DMM submechanism.<sup>8</sup> For Q4OOH radicals, analogies to the DEE intermediate were adopted and its pathways via a four- and a five-membered ring generating 2,4-dimethyl-1,3-dioxetane and 2-methyl-1,3-dioxolane, respectively.<sup>54</sup>

Furthermore, two possible thermal β-scission reactions for Q1OOHc radicals were considered (reactions class 21). The rate parameters for the reaction producing ethyl formate, ethylene, and hydroperoxyl radical are based on the corresponding reaction in the DEE mechanism by Sakai et al.<sup>54</sup> The other β-scission leads to the products ethyl radical ( $\dot{\text{C}}_2\text{H}_5$ ) and hydroperoxyethyl formate ( $\text{HO}_2\text{C}_2\text{H}_4\text{OCHO}$ ), and the A-factor is decreased by a factor of 2 compared to the corresponding β-scission reaction of R4 radical in DEM to account for the symmetry of these radicals. With the same methodology, the rate coefficients of the β-scission reaction for R2 radicals of DEM were adopted as an analogy for the

reaction  $\text{C}_2\text{H}_5\text{OCH}_2\text{OCHCH}_2\text{O}_2\text{H} \rightleftharpoons \text{C}_2\text{H}_5\text{OCH}_2 + \text{HO}_2\text{CH}_2\text{CHO}$ . The reaction rate coefficients of the Q4OOHb decomposition reaction leading to ethyl formate, acetaldehyde, and a hydroxyl radical are assigned according to the corresponding reaction in the DMM mechanism by Vermeire et al.<sup>8</sup> The activation energy was increased by 2 kcal/mol to take into account the stronger bond of the O–C–O group at the central site (88.0 kcal/mol (cf. present work) vs 86.26 kcal/mol (ref 18)). The remaining thermal β-scission reactions of reaction class 21 are adopted from the DEE submechanism by Yasunaga et al.<sup>59</sup> or have been calculated in this study.

Finally, unsaturated molecules are generated by the two QOOH radicals via HO<sub>2</sub> elimination corresponding to reaction class 20. For the Q2OOHa species with the radical site on the primary site of DEM, the rate parameters are assigned according to the corresponding reaction in the DEE mechanism by Yasunaga et al.<sup>59</sup> Neither Sakai et al.<sup>54</sup> nor Yasunaga et al.<sup>59</sup> considered the concerted elimination of HO<sub>2</sub> from the DEE equivalent Q1OOHb radical. Therefore, the rate constants are estimated from the corresponding reaction in DEE mechanism based on the recommendation of Tang et al.<sup>62</sup>

For reaction class 23, eight different reactions for the internal isomerization of O<sub>2</sub>QOOH with subsequent keto-hydroperoxide formation and release of OH are considered. The rate parameters from both DEE submechanisms<sup>54,59</sup> were used to estimate the rate coefficients for a five- and a seven-membered cyclic transition state. For isomerization reactions, which occurs through a six- and an eight-membered TS ring, the rate coefficients have been assigned in analogy to the corresponding reactions of DMM.<sup>8</sup> The variations in the structure between DEM and DMM required modification of the activation energy of –1 kcal/mol in the case of H atom shift reactions from the secondary site of the ethyl group and +0.6 kcal/mol for an internal H atom transfer from the central site. Furthermore, in the first case the A-factor is divided by a factor of 2 to take into account different number of H atoms available for abstraction.

For the decomposition of the keto-hydroperoxide (reaction class 24), the rate coefficients for the O–O fission reaction are taken from the corresponding reactions of the DMM submechanism, proposed in Jacobs et al.<sup>18</sup> For the most sensitive reaction ( $\text{C}_2\text{H}_5\text{OCH}(\text{=O})\text{OCH}(\text{OOH})\text{CH}_3 \rightleftharpoons \text{C}_2\text{H}_5\text{OCH}(\text{=O})\text{OCH}(\dot{\text{O}})\text{CH}_3 + \dot{\text{O}}\text{H}$ ) in this reaction class, a rate coefficient of  $k = 2.0 \times 10^{16} \exp(-19121 \text{ K}/T) \text{ cm}^3/\text{mol/s}$  has been assumed, which was derived from the DEE submechanism of Sakai et al.<sup>54</sup> with an activation energy decreased by 1 kcal/mol to achieve a good agreement with measured IDT in the low-temperature regime.

The rate constants for the alternative isomerization pathways of O<sub>2</sub>QOOH radicals (reaction classes 23 and 24a–d) were estimated by analogy to those for the corresponding RO<sub>2</sub> radicals. These reaction classes include the production of an unsaturated counterpart by concerted elimination of HO<sub>2</sub> and also an internal H atom transfer that yields P(OOH)<sub>2</sub> species. P(OOH)<sub>2</sub> further reacts through cyclic ether formation and a β-scission reaction.

The values of the rate coefficients of the remaining reaction classes are estimated as analogies to DMM, DEE, and *n*-heptane. The references are listed in the mechanism and in Table S7. To complete this mechanism, for the stable intermediate species diethyl carbonate, ethyl formate, and



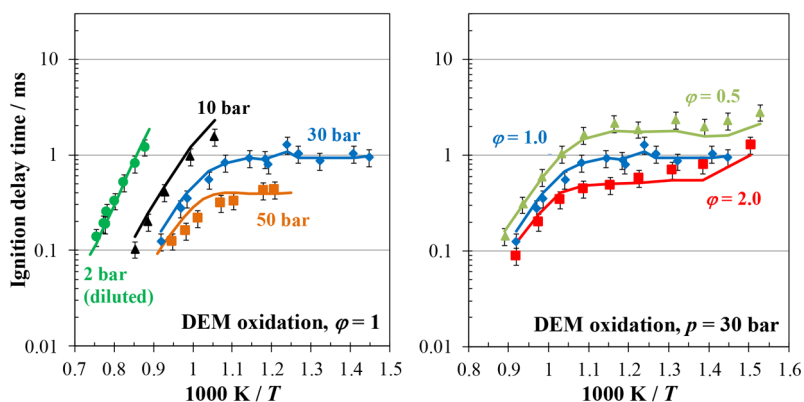


**Figure 2.** Comparison between experimental data sets (shock tube: closed symbols) and simulation results (lines) of IDTs for DEM. Diamonds: ST data of Lehrheuer et al.<sup>4</sup> at 30 bar in air; dots: ST data of Zhang et al.<sup>11</sup> at 2 bar and highly diluted; all other symbols: present work.

diethyl ether, the corresponding mechanisms from Nakamura et al.,<sup>55</sup> Sun et al.,<sup>57</sup> and Sakai et al.<sup>54</sup> have been added. Furthermore, for ethoxymethyl formate, ethoxycarbonyl formate, and formyl acetate, new submechanisms were developed and implemented in the HGD DEM mechanism. Finally, some pressure-dependent rate coefficients had to be refitted in the base mechanism to avoid a negative  $A$ -factor since the LOGEresearch simulation software suite<sup>63</sup> cannot handle this and the simulations partially did not converge. A comment was added to the base mechanism for each of these refitted reactions.

## 5. RESULTS AND DISCUSSION

The newly developed model is validated against ignition delay times (IDTs), laminar burning velocities ( $S_L$ ), and extinction strain rates ( $a_2$ ) presented herein. Further validation of the HGD DEM model has been performed against IDTs available in the literature<sup>4,11</sup> and fuel-rich premixed DEM/ethylene/oxygen/argon flames published by Dias and Vandooren.<sup>12</sup> To limit the length of this paper, some of the validation targets are presented as Supporting Information in section S4.

**5.1. Ignition Delay Times.** The experiments in the shock tube (ST) were performed from low- to high-temperature range (655–1170 K) under different pressure and equivalence ratios by using nondiluted fuel in air mixtures (Table 1). Because of the measurement range of the facility and the vapor pressure limitations of DEM, no further measurements in the low-temperature regime could be performed at 10 and 50 bar under stoichiometric conditions. To complete these new data sets, experiments at 2 and 30 bar under stoichiometric conditions for highly diluted and in-air conditions were taken from the literature<sup>4,11</sup> and are also presented in Figure 2. The experimental data sets are complemented with the corresponding simulations. For modeling the ignition behavior in the ST, the simulations were performed by using Cantera<sup>21</sup> at the experimental pressures and temperatures behind the reflected shock waves including facility effects. In addition, constant volume simulations (CVS) were performed with the LOGEresearch simulation software suite<sup>63</sup> to verify that the mechanism is compatible with other solvers. The CVS results of the predicted IDTs indicate no notable differences between the two solvers.

In contrast to dimethoxymethane, diethyl ether, long chain  $n$ -alkanes, or other highly reactive fuels, DEM shows no temperature regime where IDTs increase with increasing

temperature. Instead of the typical S-shaped behavior (negative temperature coefficient, NTC), the ignition delay of DEM in the intermediate temperature regime becomes insensitive to temperature; i.e., the chemical reactivity barely changes in this range. The scatter in IDT between  $1.2 < 1000 \text{ K}/T < 1.3$  at 30 bar under stoichiometric conditions is not due to a change in dominating chemistry but due to scattering in experimental pressures. The chemical reactivity decreases with decreasing pressure, and because of this the IDT of this data point is slightly longer compared to the others. The HGD DEM model captures the IDT measurements of the ST including the effects of various pressures, dilutions, and equivalence ratios well within the experimental uncertainties for the majority of data.

Further validations of the newly developed model against autoignition experiments of highly diluted DEM/O<sub>2</sub>/Ar mixtures in a shock tube at high temperatures under different pressures, equivalence ratios, and dilution ratios<sup>11</sup> are in Figures S7–S9.

Figure 3 depicts an overview of the ignition delay times of three different facilities, which were performed in ST, RCM,

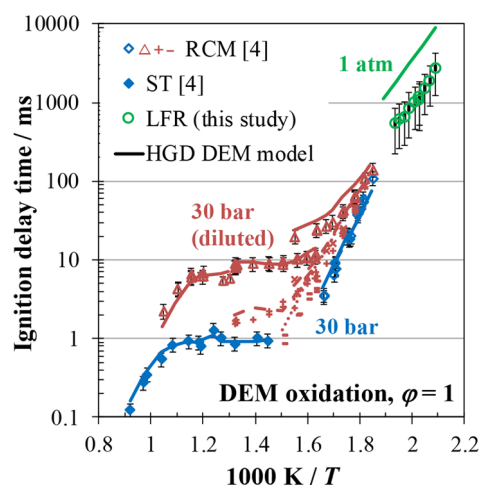


**Figure 3.** Comparison between experimental data (closed symbols: ST; open symbols: RCM and LFR) and simulation results (lines) of IDTs for DEM. Diamonds: ST and RCM data of Lehrheuer et al.<sup>4</sup> at 30 bar in air; triangles/plus/minus: main/second/first ignition RCM data of Lehrheuer et al.<sup>4</sup> at 30 bar and dilution/O<sub>2</sub> = 12; dots: LFR experiments at atmospheric pressure in air (present work).

and LFR. The measurements cover a temperature range from 480 to 1090 K for stoichiometric mixtures at atmospheric pressure and at 30 bar.

In our earlier experimental work,<sup>4</sup> we presented IDT data of DEM measured in a RCM with different diluent/O<sub>2</sub> ratios of 3.762 and 12. In addition, in the case of diluent/O<sub>2</sub> = 12, at high temperatures a bath gas composition with N<sub>2</sub> and argon was used, at intermediate temperatures only N<sub>2</sub>, and at low temperatures a N<sub>2</sub>/CO<sub>2</sub> mixture. In this study, the corresponding nonreactive experiments and more details of these new measurements are provided as [Supporting Information](#) (section S3.2) required for the simulation of these RCM data sets.<sup>4</sup>

The following is a brief review of the ignition delay time measurements performed within our previous study:<sup>4</sup> A two-stage ignition event was observed at the in-air conditions in the ST and in the RCM, with the first stage occurring immediately before the main ignition. These ignition stages before the main ignition were difficult to identify accurately, and therefore these data sets were omitted from the previous and the present evaluation. However, in the case of the higher diluted conditions, a significant multistep ignition was observed in the RCM experiments. Under these conditions, a regular two-stage ignition was measured at low temperatures. As the temperature rises, two prior ignition stages are identified before the main ignition event. At higher temperatures, again only one stage ignition before the main ignition event was detected. The multistep ignition event in the simulations of this study is defined in the same way as in Lehrheuer's work:<sup>4</sup> as the time between end-of-compression (EOC) and the maximum pressure rise determined from the pressure profiles. [Figure 4](#)

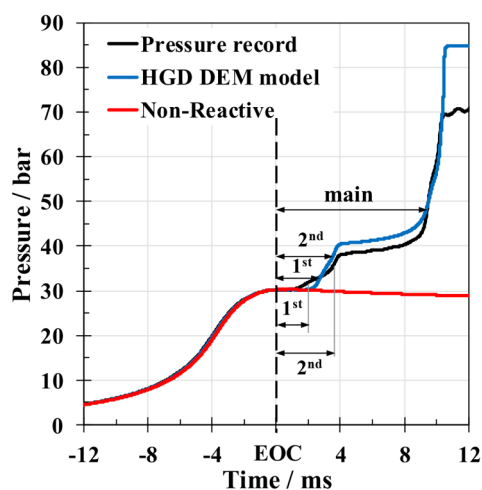


**Figure 4.** Comparison between experimental pressure history (black line)<sup>4</sup> and the predictions of the reactive (blue) and nonreactive (red) pressure histories. RCM conditions:  $p_{\text{EOC}} = 30.1$  bar,  $T_{\text{EOC}} = 641$  K, and  $\phi = 1$  at higher dilution (diluent/O<sub>2</sub> = 12).

shows the definition of ignition at higher dilution with N<sub>2</sub> as the bath gas and an EOC temperature of 641 K. In addition, the same plot depicts a comparison between the experimental pressure history and the corresponding prediction with the model.

The experimentally observed multistep ignition phenomena are qualitatively predicted by the model, but the timing and pressure rise due to the prior ignition are not always simulated perfectly. During the model development, the aforementioned

modifications to the rate coefficients (e.g., H atom abstraction by  $\dot{\text{O}}\text{H}$ ) were made to find the best compromise between the prior ignition stages and the main ignition. However, the RCM simulations slightly overpredict the IDT of the main ignition event in the low-temperature range while underpredicting IDTs for the two highest temperatures at 30 bar at higher diluted conditions. Overall, the predictions are mostly within the uncertainties of the experiments, and the kinetic mechanism developed in this study is in reasonable agreement with the RCM data sets.

Further investigation of the low-temperature ignition behavior has been performed in the LFR extending the investigation regime down to 480 K ([Figure 3](#)). Typically, the overall chemical reactivity for longer alkanes tends to converge at very low temperatures and is consequently independent of pressure and equivalence ratio. Moreover, this pressure independence has also been observed for the first-stage ignition event.<sup>25</sup> Consequently, the experiments at atmospheric pressure in the LFR are representative for low-temperature chemistry pathways of DEM oxidation. The first-stage ignition delay times in LFR conditions can be simulated by zero-dimensional homogeneous adiabatic reactor configuration by using the FlameMaster software package.<sup>64</sup> [Figure 3](#) shows a comparison of simulation results and experimental data for a stoichiometric DEM mixture under in-air conditions. The first stage IDT simulation predicts the experimental trend well, despite a slight underprediction of reactivity. In addition to these experiments, further first stage IDT has been measured in the LFR for higher diluted conditions (O<sub>2</sub>/(O<sub>2</sub> + N<sub>2</sub>) = 15%) at atmospheric pressures and is shown in [Figure S3](#). Further discussion on the relevant reaction pathways is provided in the subsequent section to guide future optimizations of the model.

## 5.2. Reaction Pathway and Sensitivity Analysis.

Detailed analyses have been performed to gain further insight into the oxidation scheme of DEM. The rate of production (ROP) and sensitivity analyses were performed at 30 bar under stoichiometric conditions in air for three different temperatures (550, 800, and 1050 K) by using a homogeneous batch reactor model at constant volume within Cantera.<sup>21</sup> The rate of production analyses were performed to identify the relevant pathways in DEM combustion. The major consumption pathways of DEM are calculated at the time when 20% of the initial fuel is consumed. The results are shown in [Figure 5](#). For brevity, reaction paths were excluded which showed <3% of flux in the entire temperature range considered.

In addition, to understand the chemistry in more detail, brute-force sensitivity analyses were performed to reveal the reactions involved in the ignition delay time prediction of DEM. In the sensitivity analysis, the  $A$ -factor of each reaction was increased ( $\tau_+$ ) and decreased ( $\tau_-$ ) by a factor of 2 to test the sensitivity of IDT ( $\tau$ ) predictions. The dimensionless sensitivity coefficient  $S$  for each reaction is then defined as  $S = \log(\tau_+/\tau_-)/\log(2.0/0.5)$ .<sup>65</sup> A positive sensitivity coefficient indicates a reactivity inhibiting effect of the respective reaction leading to an increase of IDT and vice versa for a negative sensitivity coefficient. The results of the brute-force sensitivity analysis are displayed in [Figure 6](#).

Both the ROP and the sensitivity analysis are used for a discussion of the most relevant reactions in the following. First, no influence of the unimolecular decomposition reactions on fuel consumption or ignition delay times was identified even for the highest investigated temperature at 30 bar. Only at higher temperatures and highly diluted conditions did the C–



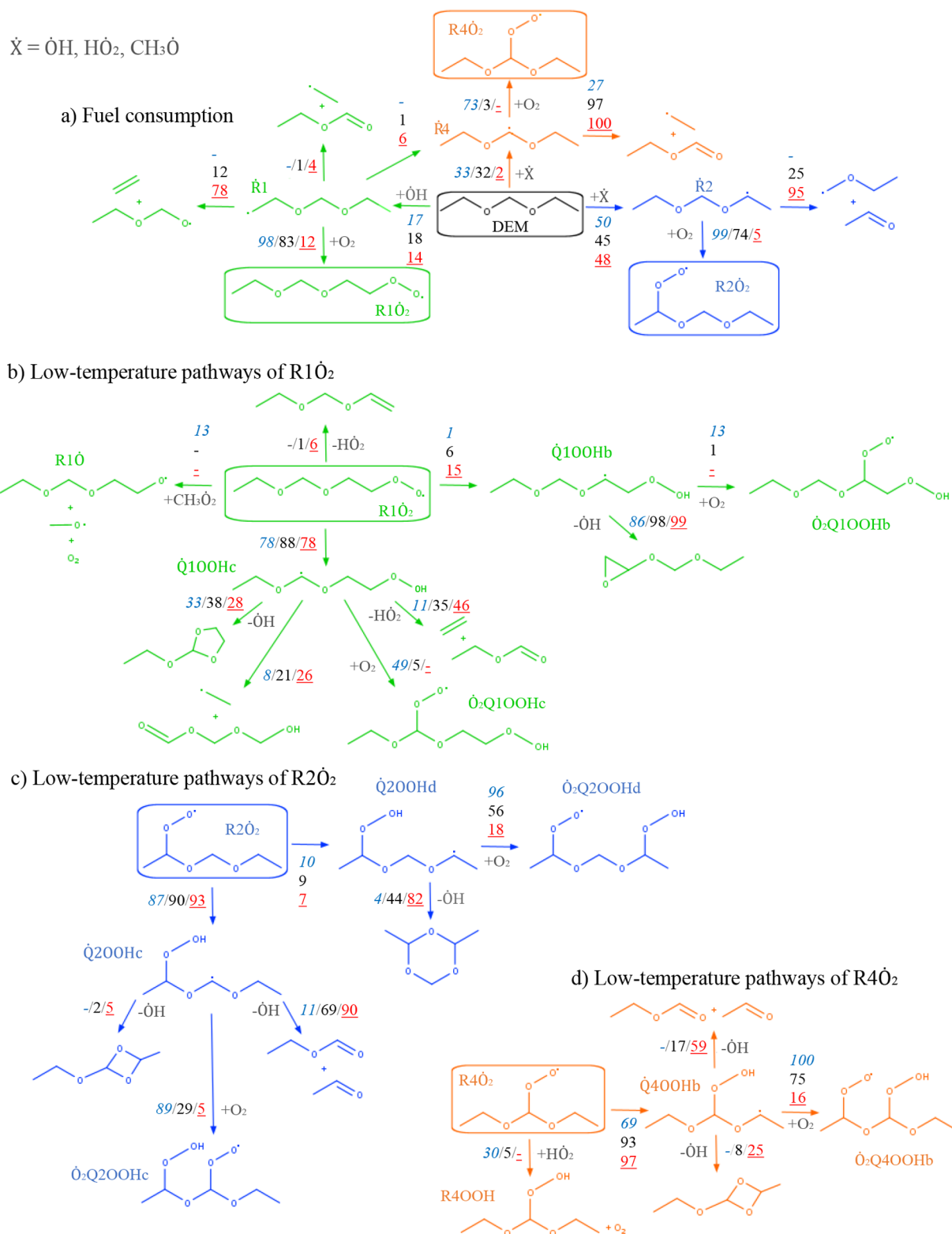


**Figure 5.** Oxidation mechanism predicted by the model for temperatures of  $T = 550$  K (blue),  $T = 800$  K (black), and  $T = 1050$  K (red) at  $p = 30$  bar under stoichiometry conditions in air. The ROP analysis was conducted at 20% fuel consumption by using a constant volume reactor.  $\dot{X}$  is the sum of  $\dot{OH}$ ,  $\dot{HO_2}$ , and  $\dot{CH_3O}$  radicals.

O bond fission reaction exhibit a significant reactivity promoting effect (Figures S10 and S11).

At 30 bar under stoichiometric conditions in air mixtures, the main consumption of DEM occurs via H atom abstraction

over the entire temperature range, resulting in the formation of the three possible DEM fuel radicals  $\dot{\text{R}}1$ ,  $\dot{\text{R}}2$ , and  $\dot{\text{R}}4$  (Figure 5a). The primary radical  $\dot{\text{R}}1$  is generated dominantly by H atom abstraction by  $\dot{\text{O}}\text{H}$  over the whole temperature range,

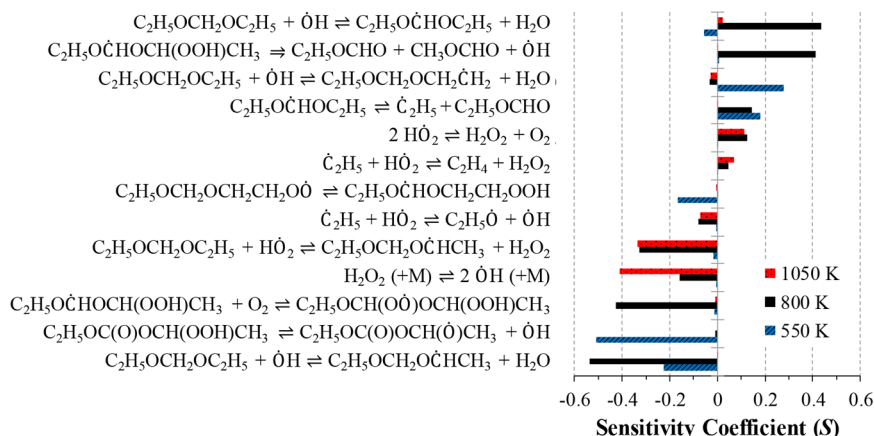


**Figure 6.** Sensitivity analyses on IDTs for a range of temperatures under stoichiometric DEM in air conditions at 30 bar as well as  $T = 550$ , 800, and 1050 K.

while abstractions on the secondary and central carbon happen by  $\dot{\text{O}}\text{H}$ ,  $\text{H}\dot{\text{O}}_2$ , and  $\text{CH}_3\dot{\text{O}}$  radicals depending on the temperature. The favored abstraction site is the secondary one due to the weak C–H bond, and the most sensitive consumption pathway is the H atom abstraction reactions by hydroxyl radicals at low and intermediate temperatures (Figure 6). At higher temperatures, however, the sensitivity shifts toward the abstraction pathway by  $\text{H}\dot{\text{O}}_2$  radicals. It is remarkable that the abstraction on the central carbon is reactivity inhibiting while the abstraction on the secondary site is reactivity enhancing at intermediate temperature. Consequently, the branching ratio between both channels is critical for modeling DEM kinetics. This behavior can be explained as follows:

After H atom abstraction, the DEM fuel radicals are consumed by the competing pathways between  $\beta$ -scission reactions and the addition to molecular oxygen. Similar to the results of DMM,<sup>8,18</sup> the fuel radical with the radical site at central carbon mainly undergoes  $\beta$ -scission reaction almost over the entire temperature range. This is caused by the low barrier height of its thermal  $\beta$ -scission cleaving the weak C–O bond at the secondary site. Therefore, alkane-like low-temperature chemical pathways toward chain branching reactions are only supported via this channel at the lowest temperature (550 K). This is different for the fuel radicals  $\dot{\text{R}}1$  and  $\dot{\text{R}}2$ . These radicals add to oxygen and are in clear competition with the thermal cleavage reactions at higher temperature. For this reason, the formation of  $\dot{\text{R}}1$  and  $\dot{\text{R}}2$  by H atom abstraction by the hydroxyl radical is overall reactivity enhancing, while it is vice versa for the  $\dot{\text{R}}4$  radical. However, the lowest temperature investigated is an exception, since the H atom abstraction on the primary site of DEM by  $\dot{\text{O}}\text{H}$  radicals shows a high positive sensitivity coefficient and thus a reactivity reducing effect (Figure 6). The reason for this shift in sensitivity is the competition with the H atom abstraction reactions producing  $\dot{\text{R}}2$  and  $\dot{\text{R}}4$  radicals which lead to effective low-temperature chain branching reactions at 550 K. Indeed,  $\text{R1O}_2$  radicals can undergo internal H atom shift via a five- and a seven-membered TS rings and not, as in the case of the other two fuel radicals, via a six-membered TS. The latter isomerization reaction via a six-membered transition is typically much faster. Therefore, the low-temperature pathways involving  $\dot{\text{R}}1$  lower the rate of  $\dot{\text{O}}\text{H}$  radical production

compared to radicals  $\dot{\text{R}}2$  and  $\dot{\text{R}}4$  and thus lead to slower fuel consumption at these conditions.

H atom abstractions by ethyl radicals do not play an important role in DEM consumption, although these radicals can be formed through different channels. However, these radicals have a non-negligible influence on the characteristic of the autoignition behavior of DEM. The ethyl radicals formed by the fast  $\beta$ -scission of  $\dot{\text{R}}4$  can subsequently add to molecular oxygen and produce ethylene and  $\text{H}\dot{\text{O}}_2$  via a concerted elimination reaction. Thus, ethyl can contribute to  $\text{H}\dot{\text{O}}_2$  formation, which is critical for the sensitive H atom abstraction by  $\text{H}\dot{\text{O}}_2$  on DEM. Furthermore, Figure 5 shows that ethyl radicals can also react further with  $\text{H}\dot{\text{O}}_2$  radicals to the products  $\text{C}_2\text{H}_4$  and  $\text{H}_2\text{O}_2$ , resulting in an inhibiting effect on reactivity at intermediate and high temperatures. However, this reaction competes with  $\dot{\text{C}}_2\text{H}_5 + \text{H}\dot{\text{O}}_2 \rightleftharpoons \text{C}_2\text{H}_5\dot{\text{O}} + \dot{\text{O}}\text{H}$ , leading to the formation of more reactive hydroxyl radicals.

Figure 5b shows that the main consumption path of the  $\text{R1O}_2$  radicals occurs via isomerization to  $\text{Q1OOHc}$  involving an internal hydrogen transfer via a seven-membered TS ring. In subsequent reactions, the second addition to  $\text{O}_2$  is part of this reaction chain, which eventually leads to the formation of two  $\dot{\text{O}}\text{H}$  radicals. This is the cause of the high negative sensitivity coefficient for this isomerization reaction (Figure 6). The importance of the consumption pathways involving the two possible  $\beta$ -scission reactions and the formation of a cyclic ether species increase with rising temperatures. Other possible consumption pathways, i.e., (i) formation of DEM alkoxy radicals ( $\text{R1O}$ ), (ii) internal isomerization reaction through a five-membered TS ring, and (iii) a concerted elimination of  $\text{H}\dot{\text{O}}_2$ , contribute only marginally to the consumption of the  $\text{R1O}_2$  radical over the entire temperature range. For this reason, it can be concluded that these reactions do not play a major role in DEM combustion.

After addition of  $\dot{\text{R}}2$  to  $\text{O}_2$ ,  $\text{R2O}_2$  radicals are mainly consumed via a six-membered TS to form  $\text{Q2OOHc}$  over the entire temperature regime. According to the ROP in Figure 5c, the second addition to  $\text{O}_2$  is dominant at low temperatures, but with increasing temperature there is a shift toward  $\beta$ -scission reaction. This competition between chain branching and chain propagation is crucial for predicting reactivity in the intermediate temperature regime as can be seen in the sensitivity analysis (Figure 6). It should be noted that the isomerization through an eight-membered transition state with

the formation of  $\dot{Q}2OOHd$  becomes negligible at high temperatures. As a result, the thermal  $\beta$ -scission path of  $\dot{Q}2OOHd$  is irrelevant and not considered in this study.

Only at the lowest temperature significant amounts of the  $R4\dot{O}_2$  radicals are identified and consumed through an isomerization reaction via a six-membered TS to  $Q4OOHb$ , followed by a second addition to oxygen and ending with the formation of two hydroxyl radicals (Figure 5d). Apart from this typical low-temperature chemistry,  $R4\dot{O}_2$  can also be consumed via  $HO_2$  radicals and decompose to alkoxy radicals ( $R4\dot{O}$ ) and hydroxyl radicals in subsequent reactions through an easy O–OH bond breaking reaction. Consequently, this path enables the conversion of  $HO_2$  radicals into more reactive OH radicals.

The sensitivity analysis indicates that one reason for the unconventional autoignition characteristic of DEM in the low to intermediate temperature regime is related to the fast  $\beta$ -scissions of  $\dot{R}4$  and  $\dot{Q}2OOHc$  ( $C_2H_5O\dot{C}HOCH(OOH)CH_3$ ) radicals. Both reactions inhibit the pathways toward low-temperature chain branching. The thermal dissociation of  $\dot{Q}2OOHc$  competes with second addition to molecular oxygen in the low-temperature pathway of  $\dot{R}2$  but becomes preferential with increasing temperature (Figure 5c). This should actually lead to a reduction in reactivity, but the ignition delay times in the intermediate temperature range remain almost constant under the conditions investigated. The reason for this is the  $HO_2/H_2O_2$  chemistry, which becomes more important with increasing temperature. The main production pathway of  $H_2O_2$  are the chain termination reaction of two  $HO_2$  with each another and the fast H atom abstraction from the secondary site of DEM. Therefore, in the case of DEM, the consumption pathway of  $HO_2$  via H atom abstraction is preferred over the self-reaction of  $HO_2$ , which usually dominates in alkane systems, for example. The reaction in which two  $HO_2$  radicals are consumed and just one  $H_2O_2$  molecule is formed subsequently leads to the formation of only two reactive OH radicals. In contrast, the H atom abstraction reaction by two  $HO_2$  produces two fuel radicals and two  $H_2O_2$  molecules, resulting in the formation of four OH radicals. This abstraction reaction involving  $\dot{R}2$  radicals subsequently leads to an increase in the rate of OH productions, resulting in faster fuel consumption and in the decrease of ignition delay time.

Moreover, the concerted elimination reactions (reaction class 12a:  $RO_2 \rightleftharpoons \text{alkene} + HO_2$ ) do not play a key role in reduction reactivity, whereas this is typically observed in the low- and intermediate-temperature chemistry of alkanes.

**5.3. Laminar Burning Velocities.** The developed mechanism is also validated against new experimental data for laminar burning velocities ( $S_L$ ) over a wide range of conditions. Some of these measured data had already been presented in advance at a conference.<sup>66</sup> The experiments were conducted at a temperature of 398 K, at atmospheric pressure and 2.5 bar, and for equivalence ratios ranging from 0.8 to 1.7 by using compressed air in a spherical combustion vessel (SCV). The experimental maximum burning velocity of 66.63 and 56.33 cm/s is recorded at an equivalence ratio of  $\phi = 1.1$  for both initial pressures. Figure 7 depicts a comparison between the experimentally obtained laminar burning velocities and the predictions of the newly developed HGD DEM model.

The freely propagating flame module in the LOGEresearch software package<sup>63</sup> is used to simulate the laminar burning velocities. The simulations included thermal diffusion and

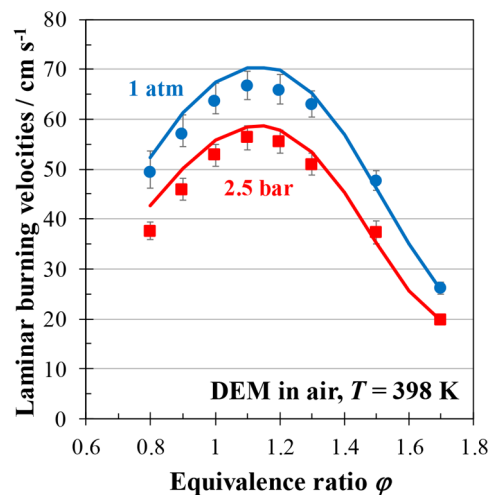


**Figure 7.** Comparison between experimental data (symbols) and simulation results (lines) of laminar burning velocities for DEM at equivalence ratios from 0.8 to 1.7 for initial temperature of 398 K at atmospheric pressure and a pressure of 2.5 bar in air.

yielded solutions for a maximum number of grid points of 301 and a maximum number of grid points per unit curvature and per unit gradient of 1.0 and 1.5, respectively. These parameters are taken from the work of Jacobs et al.<sup>18</sup> In their study the grid convergence for  $S_L$  of DMM was investigated, and accurate results were obtained with this configuration. The maximum burning velocity predictions by the kinetic model are located at an equivalence ratio of 1.15, which is slightly higher as for paraffinic fuels with a typical peak velocity position of  $1.0 \leq \phi \leq 1.1$ . For atmospheric pressure and 2.5 bar, maximum velocities of 70.35 and 58.75 cm/s are predicted, respectively. It should be noted that the laminar burning velocities were not measured at  $\phi = 1.15$  in this study. However, by following the curve progression, it indicates that the peak velocity is located between  $\phi = 1.1$  and 1.15. Comparison of laminar burning velocities from the study with diethyl ether shows that they nearly coincide with those of DEM for equivalence ratios below 1.2.<sup>67</sup> However, with increasing fuel/air ratios, DEM shows a higher  $S_L$  under fuel-rich conditions. A representative comparison at atmospheric pressure and a temperature of  $T = 398$  K is depicted in Figure S13 together with a brief discussion on the observed differences.

The simulations slightly overestimate the experimental data at atmospheric pressure for an equivalence ratio between 0.8 and 1.2, but the agreement is better with increasing equivalence ratio. Furthermore, the model achieves reasonable predictions at 2.5 bar for stoichiometric and fuel-rich conditions, while a slight deviation is observed at the fuel-lean side. The largest deviations are about 4 and 5 cm/s at an equivalence ratio of 0.9 for atmospheric pressure and an equivalence ratio of 0.8 for 2.5 bar, respectively. Nevertheless, the overall trend of the predicted burning velocities shows reasonable agreement with the experimental measurements. A sensitivity analysis was performed at equivalence ratios of 0.8, 1.15, and 1.7 for atmospheric pressure and 398 K by using the sensitivity function available in LOGEresearch.<sup>63</sup> The results indicate that most of the sensitive reactions are part of the  $C_0$ – $C_2$  base mechanism ( $O_2 + H \rightleftharpoons \dot{O} + OH$ ,  $HCO + M \rightleftharpoons CO + \dot{H} + M$ ,  $2\dot{C}H_3 \rightleftharpoons \dot{C}_2H_5 + \dot{H}$ ,  $C_2H_4 + \dot{H} + (M) \rightleftharpoons \dot{C}_2H_5 + (M)$ ,



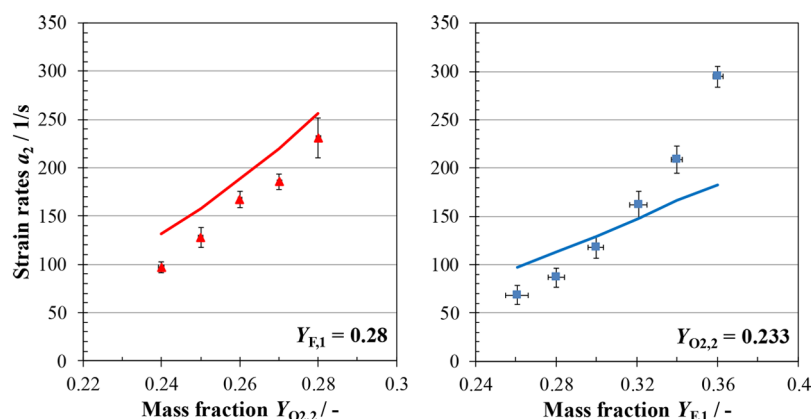


**Figure 8.** Comparison between experimental data from the counterflow burner (symbols) and simulation results (lines) for DEM. Left: extinction strain rates as a function of  $Y_{O_{2,2}}$  with constant  $Y_{F,1} = 0.28$ . Right: extinction strain rates as a function of  $Y_{F,1}$  with constant  $Y_{O_{2,2}} = 0.233$ .

$\dot{C}H_3 + (M) \rightleftharpoons C\dot{H}_4 + (M)$ ,  $CO + \dot{O}H \rightleftharpoons CO_2 + \dot{H}$ ) as can also be expected for most of hydrocarbon fuels in general. Compared to these reactions, DEM specific reactions have only a minor sensitivity to the laminar burning velocity. For this reason, no modifications of the DEM mechanism are performed to achieve a better agreement with the experimental data. A representative plot highlighting the important reactions at these conditions can be found in Figure S14.

**5.4. Extinction Strain Rates.** As additional targets, the present work provides the first extinction strain rates ( $a_2$ ) for non-premixed diffusion flames with DEM/ $N_2$  fuel and  $O_2/N_2$  oxidizer determined in a laminar counterflow burner (LFB). The measurements were performed at atmospheric pressure, and temperatures of the fuel and oxidizer streams were 405 and 305 K, respectively. The design concept with two opposite nozzles allows the mass fractions of both streams to be varied accordingly. Therefore, extinction strain rates were measured for varying fuel mass fraction  $Y_{F,1}$  at constant oxygen mass fraction  $Y_{O_{2,2}}$ , and vice versa. The results are shown in Figure 8 in comparison to the model predictions. Calculations are performed by using the FlameMaster software package.<sup>64</sup>

The model shows good performance for the prediction of the experimental data for the large strain rates at constant fuel mass fraction. However, the agreement of the experimental trend at constant oxygen mass fraction is less satisfactory. It is interesting to note that the measured large strain rates are clearly underpredicted by the model while the low strain rates are overpredicted, similar to the strain rates for small  $Y_{O_{2,2}}$  at constant fuel mass fraction. Considering all investigated conditions, the average discrepancy between experiment and simulation is 23%, with the largest discrepancy of 42% observed at constant oxygen mass fraction for the smallest  $Y_{F,1}$ . Overall, the model shows a reasonable performance although some results indicate that the model can still be improved.

**5.5. Further Data from the Literature.** For further validation of the kinetic model, the investigation of the effect of DEM addition to rich flat ethylene/oxygen/argon flames by Dias and Vandooren<sup>12</sup> were used. The comparison of the simulation results and the experimental data from ref 12 of the main and intermediate species concentrations can be found in the Supporting Information (Figure S12). The simulation results of DEM consumption achieved reasonable agreement compared to the experiments. However, the consumption of ethylene and oxygen is slightly underpredicted for high

temperature and as a consequence the simulated mole fraction profiles of some important species show discrepancies to the experimental data. To improve the prediction of the mole fractions during DEM combustion in rich ethylene flames, the subchemistry of the relevant intermediate species in the base mechanism may need to be revised in detail, which is out of the scope of this study.

Unfortunately, the performance of the previously published DEM low–high-temperature model of Li et al.<sup>17</sup> could not be tested against our RCM IDT data sets.<sup>4</sup> This is because the rate coefficients of several important reactions have been modified far beyond their uncertainties. The proposed rate parameters for the H atom abstractions by  $\dot{H}$ ,  $\dot{C}H_3$ , and  $\dot{C}_2H_5$  radicals by Li et al. are up to 6 orders of magnitude higher compared to the theoretical work of Kröger et al.<sup>16</sup> (see also Figures S24 and S25). The resulting extremely high rates induce ignition already in the precompressed initial state of the RCM simulation, which is clearly not reasonable. Furthermore, Li et al. proposed two models, both having the same high-temperature reactions, but with different rate coefficients which seems to be invalid for a consistent description of the DEM combustion kinetics. For these reasons the performance of the Li et al. mechanism is not further discussed here.

## 6. CONCLUSIONS

The present work presents a comprehensive experimental and kinetic modeling investigation involving both high- and low-temperature oxidation pathways of diethoxymethane. The new experimental data sets provide ignition delay times (IDTs), laminar burning velocities ( $S_L$ ), and extinction strain rates ( $a_2$ ) measurements. The IDTs were measured by using a shock tube under engine-relevant conditions, while the first stage IDTs were obtained from a laminar flow reactor at atmospheric pressure. The laminar burning velocities were recorded in a spherical combustion vessel from atmospheric pressure to 2.5 bar for varying equivalence ratios (0.8–1.7) at an initial temperature of 398 K. Extinction strain rates of non-premixed DEM flames were measured in a laminar counterflow burner with opposite streams of fuel/ $N_2$  (405 K) and oxidizer (305 K) under atmospheric pressure and for fuel and oxygen mass fractions of 0.26–0.36 and 0.24–0.28, respectively.

The experimental results were used to validate the newly developed kinetic reaction mechanism. Additional model validation was performed by using available literature data, i.e., various IDT investigations in a ST and RCM as well as

species measurements in a rich ethylene flame with addition of DEM. The kinetic model development includes the reaction classes relevant for high and low temperatures and is implemented on top of the C<sub>0</sub>–C<sub>4</sub> chemistry from the NUIG0.9 mechanism. In addition, the present work provides high level *ab initio* calculations for the reaction kinetics of unimolecular DEM decomposition and one relevant thermal decomposition in the low-temperature chemistry.

The autoignition characteristic of DEM is different compared to the alkanes, although the oxidation pathways are similar. Despite a multistep ignition, no NTC behavior is observed; instead, the main ignition becomes almost temperature-independent in the intermediate temperature range. The newly developed model was used to perform reaction pathway and sensitivity analyses to reveal the key reactions controlling the oxidation kinetics of DEM. They illustrate that the reactivity of DEM is largely controlled by the initial branching ratio of the production of the three fuel radicals. For the lowest temperature analyzed, all three fuel radicals can undergo alkane-like low-temperature chemistry pathways which eventually lead to chain branching. However, with increasing temperature, the diethoxymethyl radical with the radical position on the central O–C–O site is controlled by the fast  $\beta$ -scission, which has inhibitory effects on the reactivity. The unimolecular decomposition contributes only marginally to the consumption of the fuel under the condition analyzed.

To further improve the accuracy and predictive capabilities of the model, more experimental investigations and calculations of low-temperature rate constants would be required. Overall, the newly developed kinetic model is capable of predicting the experimental measurements over a wide range of conditions and represents an important improvement in the understanding of the combustion chemistry of DEM, in particular at low temperatures.

## ■ ASSOCIATED CONTENT

### ■ Supporting Information

The Supporting Information is available free of charge at <https://pubs.acs.org/doi/10.1021/acs.energyfuels.1c01988>.

Experimental description of the facilities, model performance against experimental data sets from the literature, and results of chemical kinetic modeling (PDF)

HGD DEM model in CHEMKIN format (ZIP)

Spreadsheet of the experimental data sets (XLSX)

## ■ AUTHOR INFORMATION

### Corresponding Author

**K. Alexander Heufer** – Chair of High Pressure Gas Dynamics (HGD), formerly Physico-Chemical Fundamentals of Combustion (PCFC), RWTH Aachen University, 52056 Aachen, Germany; [orcid.org/0000-0003-1657-5231](https://orcid.org/0000-0003-1657-5231); Email: [heufer@hgd.rwth-aachen.de](mailto:heufer@hgd.rwth-aachen.de)

### Authors

**Sascha Jacobs** – Chair of High Pressure Gas Dynamics (HGD), formerly Physico-Chemical Fundamentals of Combustion (PCFC), RWTH Aachen University, 52056 Aachen, Germany

**Malte Döntgen** – Chair of High Pressure Gas Dynamics (HGD), formerly Physico-Chemical Fundamentals of

Combustion (PCFC), RWTH Aachen University, 52056 Aachen, Germany

**Awad B. S. Alquaity** – Institute for Combustion Technology (ITV), RWTH Aachen University, 52056 Aachen, Germany

**Raik Hesse** – Institute for Combustion Technology (ITV), RWTH Aachen University, 52056 Aachen, Germany

**Stephan Kruse** – Institute for Combustion Technology (ITV), RWTH Aachen University, 52056 Aachen, Germany

**Joachim Beeckmann** – Institute for Combustion Technology (ITV), RWTH Aachen University, 52056 Aachen, Germany

**Leif C. Kröger** – Institute of Technical Thermodynamics (LTT), RWTH Aachen University, 52056 Aachen, Germany; [orcid.org/0000-0003-0463-1726](https://orcid.org/0000-0003-0463-1726)

**Philipp Morsch** – Chair of High Pressure Gas Dynamics (HGD), formerly Physico-Chemical Fundamentals of Combustion (PCFC), RWTH Aachen University, 52056 Aachen, Germany

**Kai Leonhard** – Institute of Technical Thermodynamics (LTT), RWTH Aachen University, 52056 Aachen, Germany

**Heinz Pitsch** – Institute for Combustion Technology (ITV), RWTH Aachen University, 52056 Aachen, Germany

Complete contact information is available at:

<https://pubs.acs.org/10.1021/acs.energyfuels.1c01988>

## Notes

The authors declare no competing financial interest.

## ■ ACKNOWLEDGMENTS

The work at the RWTH Aachen University was funded by the Deutsche Forschungsgemeinschaft (DFG, German Research Foundation) under Germany's Excellence Strategy – Exzellenzcluster 2186 “The Fuel Science Center” - ID: 390919832. The authors also thank Dr. Yann Fenard for his good advice and for insightful discussions.

## ■ REFERENCES

- (1) Leitner, W.; Klankermayer, J.; Pischinger, S.; Pitsch, H.; Kohse-Hoinghaus, K. Advanced Biofuels and Beyond: Chemistry Solutions for Propulsion and Production. *Angew. Chem., Int. Ed.* **2017**, *56* (20), 5412–5452.
- (2) Schieweck, B. G.; Klankermayer, J. Tailor-made Molecular Cobalt Catalyst System for the Selective Transformation of Carbon Dioxide to Dialkoxymethane Ethers. *Angew. Chem., Int. Ed.* **2017**, *56*, 10854–10857.
- (3) Thenert, K.; Beydoun, K.; Wiesenthal, J.; Leitner, W.; Klankermayer, J. Ruthenium-Catalyzed Synthesis of Dialkoxymethane Ethers Utilizing Carbon Dioxide and Molecular Hydrogen. *Angew. Chem., Int. Ed.* **2016**, *55*, 12266–12269.
- (4) Lehrheuer, B.; Hoppe, F.; Heufer, K. A.; Jacobs, S.; Minwegen, H.; Klankermayer, J.; Heuser, B.; Pischinger, S. Diethoxymethane as tailor-made fuel for gasoline controlled autoignition. *Proc. Combust. Inst.* **2019**, *37* (4), 4691–4698.
- (5) Fuel Science Center - FSC; available at <https://www.fuelcenter.rwth-aachen.de/cms/~siul/Fuelcenter/https://www.fuelcenter.rwth-aachen.de/cms/~siul/Fuelcenter/>, online; accessed May 2021.
- (6) Härtl, M.; Seidenspinner, P.; Jacob, E.; Wachtmeister, G. Oxygenate screening on a heavy-duty diesel engine and emission characteristics of highly oxygenated oxymethylene ether fuel OME<sub>1</sub>. *Fuel* **2015**, *153*, 328–335.
- (7) He, T.; Wang, Z.; You, X.; Liu, H.; Wang, Y.; Li, X.; He, X. A chemical kinetic mechanism for the low- and intermediate-temperature combustion of Polyoxymethylene Dimethyl Ether 3 (PODE<sub>3</sub>). *Fuel* **2018**, *212*, 223–235.
- (8) Vermeire, F. H.; Carstensen, H.-H.; Herbinet, O.; Battin-Leclerc, F.; Marin, G. B.; Van Geem, K. M. Experimental and modeling study

of the pyrolysis and combustion of dimethoxymethane. *Combust. Flame* **2018**, *190*, 270–283.

(9) Omari, A.; Heuser, B.; Pischinger, S.; Rüdinger, C. Potential of long-chain oxymethylene ether and oxymethylene ether-diesel blends for ultra-low emission engines. *Appl. Energy* **2019**, *239*, 1242–1249.

(10) Herzler, J.; Manion, J. A.; Tsang, W. Single-pulse Shock Tube Studies of the Decomposition of Ethoxy Compounds. *J. Phys. Chem. A* **1997**, *101*, 5494–5499.

(11) Zhang, C.; He, J.; Li, Y.; Li, X.; Li, P. Ignition delay times and chemical kinetics of diethoxymethane/O<sub>2</sub>/Ar mixtures. *Fuel* **2015**, *154*, 346–351.

(12) Dias, V.; Vandooren, J. Experimental and modeling studies of C<sub>2</sub>H<sub>4</sub>/O<sub>2</sub>/Ar, C<sub>2</sub>H<sub>4</sub>/methylal/O<sub>2</sub>/Ar and C<sub>2</sub>H<sub>4</sub>/ethylal/O<sub>2</sub>/Ar rich flames and the effect of oxygenated additives. *Combust. Flame* **2011**, *158*, 848–859.

(13) Porter, E.; Wenger, J.; Treacy, J.; Sidebottom, H.; Mellouki, A.; Téton, S.; LeBras, G. Kinetic Studies on the Reactions of Hydroxyl Radicals with Diethers and Hydroxyethers. *J. Phys. Chem. A* **1997**, *101* (32), 5770–5775.

(14) Thüner, L.; Barnes, I.; Maurer, T.; Sauer, C.; Becker, K. Kinetics study of the reaction of OH with a series of acetals at 298 ± 4 K. *Int. J. Chem. Kinet.* **1999**, *31* (11), 797–803.

(15) Vovelle, C.; Bonard, A.; Daële, V.; Delfau, J.-L. Kinetics of OH radical reactions with a series of symmetric acetals in the temperature range 293–617 K. *Phys. Chem. Chem. Phys.* **2001**, *3*, 4939–4945.

(16) Kröger, L. C.; Döntgen, M.; Firaha, D.; Kopp, W. A.; Leonhard, K. Ab initio kinetics predictions for H-atom abstraction from diethoxymethane by hydrogen, methyl, and ethyl radicals and the subsequent unimolecular reactions. *Proc. Combust. Inst.* **2019**, *37* (1), 275–282.

(17) Li, R.; Herreros, J. M.; Tsolakis, A.; Yang, W. Chemical kinetic modeling of diethoxymethane oxidation: A carbon-neutral fuel. *Fuel* **2021**, *291*, 120217.

(18) Jacobs, S.; Döntgen, M.; Alqaity, A. B.; Kopp, W. A.; Kröger, L. C.; Burke, U.; Pitsch, H.; Leonhard, K.; Curran, H. J.; Heufer, K. A. Detailed kinetic modeling of dimethoxymethane. Part II: Experimental and theoretical study of the kinetics and reaction mechanism. *Combust. Flame* **2019**, *205*, 522–533.

(19) Zhang, K.; Banyon, C.; Bugler, J.; Curran, H. J.; Rodriguez, A.; Herbinet, O.; Battin-Leclerc, F.; B'Chir, C.; Heufer, K. A. An updated experimental and kinetic modeling study of *n*-heptane oxidation. *Combust. Flame* **2016**, *172*, 116–135.

(20) Shepherd, J. E. Shock and detonation toolbox, available at <http://shepherd.caltech.edu/EDL/PublicResources/sdt/>, online; accessed May 2021.

(21) Goodwin, D. G.; Moffat, H. K.; Speth, R. L. Cantera: An Object-oriented Software Toolkit for Chemical Kinetics, Thermodynamics, and Transport Processes. Version 2.4.0, available at [www.cantera.org](http://www.cantera.org), online; accessed May 2021.

(22) Petersen, E. L.; Hanson, R. K. Nonideal effects behind reflected shock waves in a high-pressure shock tube. *Shock waves* **2001**, *10* (6), 405–420.

(23) Heufer, K. A.; Bugler, J.; Curran, H. J. A comparison of longer alkane and alcohol ignition including new experimental results for *n*-pentanol and *n*-hexanol. *Proc. Combust. Inst.* **2013**, *34*, 511–518.

(24) Burke, S. M.; Burke, U.; Mc Donagh, R.; Mathieu, O.; Osorio, I.; Keese, C.; Morones, A.; Petersen, E. L.; Wang, W.; DeVerter, T. A.; Oehlschlaeger, M. A.; Rhodes, B.; Hanson, R. K.; Davidson, D. F.; Weber, B. W.; Sung, C.-J.; Santner, J.; Ju, Y.; Haas, F. M.; Dryer, F. L.; Volkov, E. N.; Nilsson, E. J.; Konnov, A. A.; Alrefae, M.; Khaled, F.; Farooq, A.; Dirrenberger, P.; Glaude, P.-A.; Battin-Leclerc, F.; Curran, H. J. An experimental and modeling study of propene oxidation. Part 2: Ignition delay time and flame speed measurements. *Combust. Flame* **2015**, *162* (2), 296–314.

(25) Sudholt, A.; Cai, L.; Pitsch, H. Laminar flow reactor experiments for ignition delay time and species measurements at low temperatures: Linear alkanes and dimethyl ether. *Combust. Flame* **2019**, *202*, 347–361.

(26) Wada, T.; Sudholt, A.; Pitsch, H.; Peters, N. Analysis of first stage ignition delay times of dimethyl ether in a laminar flow reactor. *Combust. Theory Modell.* **2013**, *17* (5), 906–934.

(27) Beeckmann, J.; Cai, L.; Pitsch, H. Experimental investigation of the laminar burning velocities of methanol, ethanol, *n*-propanol, and *n*-butanol at high pressure. *Fuel* **2014**, *117*, 340–350.

(28) Settles, G. S. *Schlieren and Shadowgraph Techniques: Visualizing Phenomena in Transparent Media*; Springer-Verlag: Berlin, 2001.

(29) Chen, Z.; Burke, M.; Ju, Y. Effects of Lewis number and ignition energy on the determination of laminar flame speed using propagating spherical flames. *Proc. Combust. Inst.* **2009**, *32*, 1253–1260.

(30) Bradley, D.; Gaskell, P.; Gu, X. Burning velocities, markstein lengths, and flame quenching for spherical methane-air flames: A computational study. *Combust. Flame* **1996**, *104*, 176–198.

(31) Matalon, M.; Matkowsky, B. Flames as gasdynamic discontinuities. *J. Fluid Mech.* **1982**, *124*, 239–259.

(32) Wu, C.; Law, C. On the determination of laminar flame speeds from stretched flames. *Symp. (Int.) Combust., [Proc.]* **1985**, *20*, 1941–1949.

(33) Kelley, A.; Bechtold, J.; Law, C. Premixed flame propagation in a confining vessel with weak pressure rise. *J. Fluid Mech.* **2012**, *691*, 26–51.

(34) JCGM *Evaluation of measurement data - guide to the expression of uncertainty in measurement*, Geneva, ISBN **2008**, 50, 134.

(35) Cai, L.; Kruse, S.; Felsmann, D.; Thies, C.; Yalamanchi, K. K.; Pitsch, H. Experimental Design for Discrimination of Chemical Kinetic Models for Oxy-Methane Combustion. *Energy Fuels* **2017**, *31* (5), 5533–5542.

(36) Kruse, S.; Wick, A.; Medwell, P.; Attili, A.; Beeckmann, J.; Pitsch, H. Experimental and numerical study of soot formation in counterflow diffusion flames of gasoline surrogate component. *Combust. Flame* **2019**, *210*, 159–171.

(37) Stephens, P.; Devlin, F.; Chabalowski, C.; Frisch, M. Ab Initio Calculation of Vibrational Absorption and Circular Dichroism Spectra Using Density Functional Force Fields. *J. Phys. Chem.* **1994**, *98*, 11623–11627.

(38) Grimme, S.; Ehrlich, S.; Goerigk, L. Effect of the damping function in dispersion corrected density functional theory. *J. Comput. Chem.* **2011**, *32*, 1456–1465.

(39) Riplinger, C.; Pinski, P.; Becker, U.; Valeev, E.; Neese, F. Sparse maps - A systematic infrastructure for reduced-scaling electronic structure methods. II. Linear scaling domain based pair natural orbital coupled cluster theory. *J. Chem. Phys.* **2016**, *144*, 024109.

(40) Saitow, M.; Becker, U.; Riplinger, C.; Valeev, E.; Neese, F. A new near-linear scaling, efficient and accurate, open-shell domain-based local pair natural orbital coupled cluster singles and doubles theory. *J. Chem. Phys.* **2017**, *146*, 164105.

(41) Halkier, A.; Helgaker, T.; Jørgensen, P.; Klopper, W.; Koch, H.; Olsen, J.; Wilson, A. Basis-set convergence in correlated calculations on Ne, N<sub>2</sub>, and H<sub>2</sub>O. *Chem. Phys. Lett.* **1998**, *286*, 243–252.

(42) Neese, F. The orca program system, Wiley interdisciplinary Reviews - Computational Molecular. *Wiley Interdiscip. Rev.: Comput. Mol. Sci.* **2012**, *2*, 73–78.

(43) Frisch, M. J.; Trucks, G. W.; Schlegel, H. B.; Scuseria, G. E.; Robb, M. A.; Cheeseman, J. R.; Scalmani, G.; Barone, V.; Petersson, G. A.; Nakatsuji, H.; Li, X.; M., C.; Marenich, A. V.; Bloino, J.; Janesko, B. G.; Gomperts, R.; Mennucci, B.; Hratchian, H. P.; Ortiz, J. V.; Izmaylov, A. F.; Sonnenberg, J. L.; Williams-Young, D.; Ding, F.; Lipparini, F.; Egidi, F.; Goings, J.; Peng, B.; Petrone, A.; Henderson, T.; Ranasinghe, D.; Zakrzewski, V. G.; Gao, J.; Rega, N.; Zheng, G.; Liang, W.; Hada, M.; Ehara, M.; Toyota, K.; Fukuda, R.; Hasegawa, J.; Ishida, M.; Nakajima, T.; Honda, Y.; Kitao, O.; Nakai, H.; Vreven, T.; Throssell, K.; Montgomery, J. A., Jr.; Peralta, J. E.; Ogliaro, F.; Bearpark, M. J.; Heyd, J. J.; Brothers, E. N.; Kudin, K. N.; Staroverov, V. N.; Keith, T. A.; Kobayashi, R.; Normand, J.; Raghavachari, K.; Rendell, A. P.; Burant, J. C.; Iyengar, S. S.; Tomasi, J.; Cossi, M.; Millam, J. M.; Klene, M.; Adamo, C.; Cammi, R.; Ochterski, J. W.;



- Martin, R. L.; Morokuma, K.; Farkas, O.; Foresman, J. B.; Fox, D. J. *Gaussian 16*, Rev. B.01; Gaussian Inc.: Wallingford, CT, 2016.
- (44) Georgievskii, Y.; Miller, J.; Burke, M.; Klippenstein, S. Reformulation and Solution of the Master Equation for Multiple-Well Chemical Reactions. *J. Phys. Chem. A* **2013**, *117*, 12146–12154.
- (45) Gao, C.; Allen, J.; Green, W.; West, R. Reaction Mechanism Generator: Automatic construction of chemical kinetic mechanisms. *Comput. Phys. Commun.* **2016**, *203*, 212–225.
- (46) Tee, L.; Gotoh, S.; Stewart, W. Molecular Parameters for Normal Fluids. Lennard-Jones 12–6 Potential. *Ind. Eng. Chem. Fundam.* **1966**, *5*, 356–363.
- (47) Lizardo-Huerta, J.-C.; Sirjean, B.; Glaude, P.-A.; Fournet, R. Pericyclic reactions in ether biofuels. *Proc. Combust. Inst.* **2017**, *36* (1), 569–576.
- (48) Bugler, J.; Somers, K. P.; Silke, E. J.; Curran, H. J. Revisiting the Kinetics and Thermodynamics of the Low-Temperature Oxidation Pathway of Alkane: A Case Study of the Three Pentane Isomers. *J. Phys. Chem. A* **2015**, *119*, 7510–7527.
- (49) Villano, S. M.; Huynh, L. K.; Carstensen, H.-H.; Dean, A. M. High-Pressure Rate Rules for Alkyl + O<sub>2</sub> Reactions. 1. The Dissociation, Concerted Elimination, and Isomerization Channels of the Alkyl Peroxy Radical. *J. Phys. Chem. A* **2011**, *115*, 13425–13442.
- (50) Villano, S.; Huynh, L.; Carstensen, H.; Dean, A. High-Pressure Rate Rules for Alkyl + O<sub>2</sub> Reactions. 2. The Isomerization, Cyclic Ether Formation, and  $\beta$ -Scission Reactions of Hydroperoxy Alkyl Radicals. *J. Phys. Chem. A* **2012**, *116*, 5068–5089.
- (51) Goldsmith, C.; Burke, M.; Georgievskii, Y.; Klippenstein, S. Effect of non-thermal product energy distributions on ketohydroperoxide decomposition kinetics. *Proc. Combust. Inst.* **2015**, *35*, 283–290.
- (52) Döntgen, M.; Kopp, W. A.; vom Lehn, F.; Kröger, L. C.; Pitsch, H.; Leonhard, K.; Heufer, K. A. Updated thermochemistry for renewable transportation fuels: New groups and group values for acetals and ethers, their radicals, and peroxy species. *Int. J. Chem. Kinet.* **2021**, *53*, 299–307.
- (53) Ritter, E. R.; Bozzelli, J. W. THERM: Thermodynamic property estimation for gas phase radicals and molecules. *Int. J. Chem. Kinet.* **1991**, *23*, 767–778.
- (54) Sakai, Y.; Herzler, J.; Werler, M.; Schulz, C.; Fikri, M. A quantum chemical and kinetics modeling study on the autoignition mechanism of diethyl ether. *Proc. Combust. Inst.* **2017**, *36* (1), 195–202.
- (55) Nakamura, H.; Curran, H. J.; Polo Córdoba, A.; Pitz, W. J.; Dagaut, P.; Togbé, C.; Sarathy, S. M.; Mehl, M.; Agudelo, J. R.; Bustamante, F. An experimental and modeling study of diethyl carbonate oxidation. *Combust. Flame* **2015**, *162*, 1395–1405.
- (56) Joshi, A.; You, X.; Barckholtz, T. A.; Wang, H. Thermal Decomposition of Ethylene Oxide: Potential Energy Surface, Master Equation Analysis, and Detailed Kinetic Modeling. *J. Phys. Chem. A* **2005**, *109* (35), 8016–8027.
- (57) Sun, W.; Tao, T.; Zhang, R.; Liao, H.; Huang, C.; Zhang, F.; Zhang, X.; Zhang, Y.; Yang, B. Experimental and modeling efforts towards a better understanding of the high-temperature combustion kinetics of C<sub>3</sub>–C<sub>5</sub> ethyl esters. *Combust. Flame* **2017**, *185*, 173–187.
- (58) Baigmohammadi, M.; Patel, V.; Martinez, S.; Panigrahy, S.; Ramalingam, A.; Burke, U.; Somers, K. P.; Heufer, K. A.; Pekalski, A.; Curran, H. J. A Comprehensive Experimental and Simulation Study of Ignition Delay Time Characteristics of Single Fuel C<sub>1</sub>–C<sub>2</sub> Hydrocarbons over a Wide Range of Temperatures, Pressures, Equivalence Ratios, and Dilutions. *Energy Fuels* **2020**, *34*, 3755–3771.
- (59) Yasunaga, K.; Simmie, J. M.; Curran, H. J.; Koike, T.; Takahashi, O.; Kuraguchi, Y.; Hidaka, Y. Detailed chemical kinetic mechanisms of ethyl methyl, methyl *tert*-butyl and ethyl *tert*-butyl ethers: The importance of uni-molecular elimination reactions. *Combust. Flame* **2011**, *158*, 1032–1036.
- (60) Kopp, W. A.; Kröger, L. C.; Döntgen, M.; Jacobs, S.; Burke, U.; Curran, H. J.; Heufer, K. A.; Leonhard, K. Detailed kinetic modeling of dimethoxymethane. Part I: Ab initio thermochemistry and kinetics predictions for key reactions. *Combust. Flame* **2018**, *189*, 433–442.
- (61) Alzueta, M. U.; Aranda, V.; Monge, F.; Millera, A.; Bilbao, R. Oxidation of methyl formate and its interaction with nitric oxide. *Combust. Flame* **2013**, *160*, 853–860.
- (62) Tang, Z.; Zhang, L.; Chen, X.; Tang, G. Improved Kinetic Mechanism for Diethyl Ether Oxidation with a Reduced Model. *Energy Fuels* **2017**, *31*, 2803–2813.
- (63) LOGEresearch, available at <http://logesoft.com/loges-software/>, online; accessed May 2021.
- (64) Pitsch, H. A C++ computer program for 0D combustion and 1D laminar flame calculations, available at <http://www.itv.rwth-aachen.de/downloads/flammemaster/>, online; accessed May 2021.
- (65) Burke, U.; Somers, K. P.; O'Toole, P.; Zinner, C. M.; Marquet, N.; Bourque, G.; Petersen, E. L.; Metcalfe, W. K.; Serinyel, Z.; Curran, H. J. An ignition delay and kinetic modeling study of methane, dimethyl ether, and their mixtures at high pressures. *Combust. Flame* **2015**, *162*, 315–330.
- (66) Kopp, W.; Kröger, L. C.; Cai, L.; Hesse, R.; Kruse, S.; Alqaity, A. B.; Beeckmann, J.; Jacobs, S.; Minwegen, H.; Heufer, K. A.; Pitsch, H.; Leonhard, K. Combustion Chemistry of Diethoxymethane (DEM): Experiments, Theory and Modeling, in: 6<sup>th</sup> International Conferenz of Tailor-Made Fuels - From Production to Propulsion, June 19–21, Aachen, Germany, 2018.
- (67) Gillespie, F.; Metcalfe, W. K.; Dirrenberger, P.; Herbinet, O.; Glaude, P.-A.; Battin-Leclerc, F.; Curran, H. J. Measurements of flat-flame velocities of diethyl ether in air. *Energy* **2012**, *43*, 140–145.